A data-model approach to interpreting speleothem oxygen isotope records from monsoon regions on orbital timescales

Sarah E. Parker[1], Sandy P. Harrison[1], Laia Comas-Bru[1], Nikita Kaushal[2], Allegra N. LeGrande[3], Martin Werner[4]

5   [1]School of Archaeology, Geography and Environmental Science, Reading University, Reading, UK
[2]Asian School of the Environment, Nanyang Technological University, Singapore
[3]NASA Goddard Institute for Space Studies and Center for Climate Systems Research, Columbia University, New York, USA
[4]Alfred Wegener Institute, Helmholtz Centre for Polar and Marine Research, Bremerhaven, Germany

Correspondence to: Sarah E. Parker (s.parker@pgr.reading.ac.uk)

10   **Abstract.** Reconstruction of past changes in monsoon climate from speleothem oxygen isotope (δ^{18}O) records is complex because δ^{18}O signals can be influenced by multiple factors including changes in precipitation, precipitation recycling over land, temperature at the moisture source and changes in the moisture source region and transport pathway. Here, we analyse >150 speleothem records from version 2 of the Speleothem Isotopes Synthesis and Analysis (SISAL) database to produce composite regional trends in δ^{18}O in monsoon regions; compositing minimises the influence of site-specific karst and cave

15   processes that can influence individual site records. We compare speleothem δ^{18}O observations with isotope-enabled climate model simulations to investigate the specific climatic factors causing these regional trends. We focus on differences in δ^{18}O signals between interglacial (mid-Holocene and Last Interglacial) and glacial (Last Glacial Maximum) states, and on δ^{18}O evolution through the Holocene. Differences in speleothem δ^{18}O between the mid-Holocene and Last Interglacial in the East Asian and Indian monsoons are small, despite the larger summer insolation values during the Last Interglacial. Last Glacial

20   Maximum δ^{18}O values are significantly less negative than interglacial values. Comparison with simulated glacial-interglacial δ^{18}O shows that changes are principally driven by global shifts in temperature and regional precipitation. Holocene speleothem δ^{18}O records show distinct and coherent regional trends. Trends are similar to summer insolation in India, China and southwestern South America, but different in the Indonesian-Australian region. Redundancy analysis shows that 37% of Holocene variability can be accounted for by latitude and longitude, supporting the differentiation of records into individual

25   monsoon regions. Regression analysis of simulated precipitation δ^{18}O and climate variables show that global Holocene monsoon δ^{18}O trends are driven by changes in precipitation, atmospheric circulation and (to a lesser extent) source area temperature, whilst precipitation recycling is non-significant. However, there are differences in regional scale mechanisms; there are clear relationships between changes in precipitation and in δ^{18}O for India, southwestern South America and the Indonesian-Australian regions, but not for the East Asian monsoon. Changes in atmospheric circulation contributes to δ^{18}O

30   trends in the East Asian, Indian and Indonesian-Australian monsoons, and a weak source area temperature effect is observed over southern and central America and Asia. Precipitation recycling is influential in southwestern South America and southern

Africa. Overall, our analyses show that it is possible to differentiate the impacts of specific climatic mechanisms influencing precipitation $\delta^{18}O$ and use this analysis to interpret changes in speleothem $\delta^{18}O$.

1 Introduction

35 The oxygen isotopic ($\delta^{18}O$: $^{18}O/^{16}O$ ratio relative to a standard, in permil, ‰) composition of speleothems is widely used to infer past regional climates (Bar-Matthews et al., 1997; McDermott, 2004; Wang et al., 2008). Speleothem oxygen isotope ($\delta^{18}O_{spel}$) signals are inherited from $\delta^{18}O$ in precipitation ($\delta^{18}O_{precip}$) above the cave, which in turn is determined by the initial $\delta^{18}O$ of water vapour as it evaporates at the oceanic moisture source region, the degree of rainout and evaporation from source to cave site and air temperature changes encountered throughout the moisture transport pathway (Fairchild and Baker, 2012;

40 Lachniet, 2009). Understanding the effects and contribution of each of these climate processes to $\delta^{18}O_{precip}$ (and therefore $\delta^{18}O_{spel}$) is essential to inferring palaeoclimate from speleothem $\delta^{18}O$ records.

Initial $\delta^{18}O$ is determined by oceanic $\delta^{18}O$ at the evaporative moisture source region (Craig and Gordon, 1965), which varies spatially (LeGrande and Schmidt, 2006) and through time (e.g. Waelbroeck et al., 2002). During evaporation from the moisture source, ^{16}O is preferentially incorporated into the vapour, whilst subsequent fractionation during atmospheric transport occurs

45 by Rayleigh distillation; As air masses cool and moisture condenses, heavier ^{18}O is enriched in the liquid phase and removed by precipitation. With progressive rainout along a moisture pathway, precipitation becomes gradually more depleted (Dansgaard, 1964). Within this framework, $\delta^{18}O_{precip}$ is controlled by two variables: temperature and the amount of precipitation along a moisture pathway. The temperature effect stems from the temperature dependence of oxygen isotope fractionation during condensation and the cooling required for rainout (Dansgaard, 1964; Rozanski et al., 1993). The

50 temperature-$\delta^{18}O$ impact is dominant at mid to high latitudes whilst at tropical latitudes, observations suggest that changes in upstream and local precipitation dominate changes in the $\delta^{18}O_{precip}$ signal. The negative relationship between local precipitation and $\delta^{18}O_{precip}$, often referred to as the "amount effect" (Bailey et al., 2018; Dansgaard, 1964), results from the re-evaporation and diffusive exchange between precipitation and water vapour during deep convective precipitation (Risi et al., 2008). However, Rayleigh distillation is complicated by changes in atmospheric circulation and moisture recycling. Changes in the

55 area from which the moisture is sourced will modify $\delta^{18}O_{precip}$ because the initial $\delta^{18}O$ values differ between sources (Cole et al., 1999; Friedman et al., 2002), whilst changes in the moisture transport pathway and/or distance between source and cave site can result in differing degrees of fractionation associated with condensation and evaporation (Aggarwal et al., 2012; Bailey et al., 2018). The isotopic composition of atmospheric water vapour may also be modified by precipitation recycling over land, since evapotranspiration returns depleted $\delta^{18}O$ from precipitation back to the atmosphere thereby reducing the

60 $\delta^{18}O_{precip}$/distance gradient along an advection path that occurs with Rayleigh distillation (Gat, 1996; Salati et al., 1979).

Speleothem $\delta^{18}O$ records from monsoon regions show multi-millennial variability that has been interpreted as documenting the waxing and waning of the monsoons in response to changes in summer insolation, manifested as either a change in the absolute amount of precipitation (Cai et al., 2012; Cheng et al., 2006) or a change in the ratio of more negative $\delta^{18}O$ summer

precipitation to less negative δ^{18}O winter precipitation (Cruz et al., 2005; Dong et al., 2010; Wang et al., 2001). However, the
65   multiplicity of processes that influence δ^{18}O before incorporation in the speleothem make it difficult to attribute the climatic
causes of changes in individual speleothem records unambiguously. In the East Asian monsoon, for example, speleothem δ^{18}O
records have been interpreted as regional rainfall signals (Cheng et al., 2006, 2009; Wang et al., 2001; Yuan et al., 2004) based
on the relationship between modern $\delta^{18}O_{precip}$ and climate. However, Maher (2008) interpreted $\delta^{18}O_{spel}$ as reflecting changes in
moisture source area, based on differences between $\delta^{18}O_{spel}$ and loess/palaeosol records of rainfall and the strong correlation
70   between East Asian and Indian monsoon speleothems. Maher and Thompson (2012) used a mass balance approach to show
that the change in precipitation required to reproduce the observed changes in $\delta^{18}O_{spel}$ was unreasonably large even if the
effects of seasonality and temperature were considered. They therefore argued that changes in moisture source were required
to explain shifts in δ^{18}O both on glacial/interglacial time scales and during interglacials. There are also conflicting
interpretations of the causes of $\delta^{18}O_{spel}$ variability in other monsoon regions. In the Indonesian-Australian monsoon region, for
75   example, $\delta^{18}O_{spel}$ variability has been interpreted as both a precipitation amount signal (Carolin et al., 2016; Krause et al., 2019)
and as a result of changing moisture source regions (Griffiths et al., 2009; Wurtzel et al., 2018). South American speleothem
records have been interpreted as records of monsoon intensity, either due to a change in the amount of precipitation, based on
relationships derived from instrumental data (Hardy et al., 2003) or due to changes in the ratio of precipitation sourced from
the low-level jet versus the Atlantic (Cruz et al., 2005; Wang et al., 2006).

80   The sources of $\delta^{18}O_{spel}$ variability have been explored using isotope-enabled climate models. Modelling studies (e.g. LeGrande
and Schmidt, 2009; Lewis et al., 2010; Pausata et al., 2011) suggest that past changes in $\delta^{18}O_{precip}$ do not reflect local rainfall
variability in the East Asian monsoon but instead reflect changes in δ^{18}O of vapour delivered to a region, consistent with
interpretation by Maher (2008). Variability in the δ^{18}O of vapour on orbital timescales has been attributed to changes in
precipitation upstream of the region (Battisti et al., 2014), changes in moisture source location (Hu et al., 2019; Tabor et al.,
85   2018) or changes in the strength of monsoon winds (LeGrande and Schmidt, 2009; Liu et al., 2014). $\delta^{18}O_{precip}$ variability in the
East Asian monsoon during Heinrich events has also been attributed to non-local isotope fractionation (Lewis et al., 2010;
Pausata et al., 2011). Modelling results generally support the qualitative interpretations of speleothem records from other
regions, suggesting that changes in precipitation amount are the predominant source of δ^{18}O variability in the Indian monsoon
during the Holocene (LeGrande and Schmidt, 2009) and in the glacial (Lewis et al., 2010), and in the South American and
90   Indonesian/Australian regions during Heinrich events (Lewis et al., 2010) and the Last Interglacial (Sjolte and Hoffman, 2014).
In this study, we combine speleothem δ^{18}O records from version 2 of the Speleothem Synthesis and Analysis (SISAL) database
with isotope-enabled palaeoclimate simulations from two climate models to investigate the causes of changes in δ^{18}O in
monsoon regions through the Holocene (last 11,700 years) and between interglacial (mid-Holocene and Last Interglacial) and
glacial (Last Glacial Maximum) states. We compare $\delta^{18}O_{spel}$ signals across geographically separated cave sites to extract a
95   regional signal, thus minimising the influence of karst and in-cave processes, such as the mixing of groundwaters from different
precipitation events or changes in cave ventilation, that can be important for the $\delta^{18}O_{spel}$ of individual records. We use Principal
Coordinate Analysis (PCoA) to identify regions with geographically coherent $\delta^{18}O_{spel}$ records, and then examine how these

regions behave on glacial-interglacial time scales and through the Holocene. We use isotope-enabled model simulations, where the processes that influence $\delta^{18}O_{precip}$ are explicitly simulated, to investigate the main drivers of regional $\delta^{18}O_{spel}$ variability.

100 We also use multiple regression analysis to identify the likely causes of the observed $\delta^{18}O_{precip}$ changes and trends in specific monsoon regions.

2. Methods

2.1 Speleothem oxygen isotope data

Speleothem $\delta^{18}O$ records were obtained from the SISAL (Speleothem Isotopes Synthesis and Analysis) database

105 (Atsawawaranunt et al., 2018; Comas-Bru et al., 2020a, 2020b). Records were selected based on the following criteria:

- They are located in monsoon regions, between 35°S and 40°N;
- The mineralogy is known but does not vary (i.e. between calcite and aragonite) through time, because oxygen isotope fractionation during speleothem precipitation is different for calcite and aragonite;
- For the interglacial-glacial analyses, the records contain samples in the periods used for the model simulations: mid-
110 Holocene (MH, 6,000±500 years BP, 6ka), Last Glacial Maximum (LGM, 21,000±1,000 years BP, 21ka) or the Last Interglacial (LIG, 125,000±1,000 years BP, 125 ka), where BP (before present) is 1950 CE;
- For the Principal Coordinate Analysis (PCoA), the records have a temporal coverage of at least 4,000 years in the Holocene;
- For Holocene trend analyses, speleothems have a record of the period from 7,000 to 3,000 years BP;
115 - They are the most recent update of the record from a site available in version 2 of the SISAL database.

This resulted in the selection of 125 records from 44 sites for the PCoA analysis, 64 records from 38 sites for the analysis of MH, LGM and LIG signals and 79 records from 40 sites for the Holocene trend analysis (Fig. 1). Although the SISALv2 database contains multiple age models for some sites, we use the published age models given by the original authors for all records.

120 **2.2 Climate model simulations**

We use two isotope-enabled climate models: ECHAM5 and GISS E-R. We used published simulations from the ECHAM5 climate model, run either in atmosphere-only (Werner et al., 2011) or in fully coupled mode (Gierz et al., 2017b; Werner et al., 2016) to investigate $\delta^{18}O$ signals during the MH, LGM and LIG. The GISS Model E-R Ocean-Atmosphere Coupled General Circulation Model (LeGrande and Schmidt, 2009) was used to investigate Holocene $\delta^{18}O$ evolution as multiple

125 isotope-enabled Holocene time-slice experiments exist. There are relatively few paleoclimate simulations made with models that incorporate oxygen isotope tracers, and the available simulations do not necessarily use the same modelling protocols. However, two sets of isotope-enabled simulations used here generally conform with PMIP (Paleoclimate Modelling Intercomparison Project) protocols, using reasonable and recommended boundary conditions (trace gases, orbital configuration etc).

130 The ECHAM5-wiso MH experiment (Wackerbarth et al., 2012; Werner, 2019) was forced by orbital parameters (based on Berger and Loutre, 1991) and greenhouse gas (GHG) concentrations (CO_2 = 280 ppm, CH_4 = 650 ppb, N_2O = 270 ppb)

appropriate to 6 ka. Changes in sea-surface temperature (SST) and sea-ice were derived from a transient Holocene simulation (Varma et al., 2012). The control simulation for the MH experiment was an ECHAM-wiso simulation of the period 1956-1999 (Langebroek et al., 2011), using observed SSTs and sea-ice cover. This control experiment was forced by SSTs and sea-ice

135   only, with atmospheric circulation free to evolve. The ECHAM5-wiso LGM experiment (Werner, 2019; Werner et al., 2018) was forced by orbital parameters (Berger and Loutre, 1991), GHG concentrations (CO_2 = 185 ppm, CH_4 = 350 ppb, N_2O = 200 ppb), land-sea distribution and ice sheet height and extent appropriate to 21 ka; SST and sea-ice cover were prescribed from the GLAMAP dataset (Schäfer-Neth and Paul, 2003). Sea surface water and sea-ice $\delta^{18}O$ were uniformly enriched by 1 ‰ at the start of the experiment. The control simulation for the LGM experiment used present-day conditions, including orbital

140   parameters and GHG concentrations set to modern values, and SSTs and sea-ice cover from the last 20 years (1979-1999). Both the MH and LGM simulations were run at T106 horizontal grid resolution, approximately 1.1° by 1.1°. The LIG experiment (Gierz et al., 2017b, 2017a) was run using the ECHAM5/MPI-OM Earth System Model, with stable water isotope diagnostics included in the ECHAM5 atmosphere model (Werner et al., 2011), the dynamic vegetation model JSBACH (Haese et al., 2012) and the MPI-OM ocean/sea-ice module (Xu et al., 2012). This simulation was run at a T31L19 horizontal grid

145   resolution, approximately 3.75° by 3.75°. The LIG simulation was forced by orbital parameters derived from the Berger and Loutre (1991) solution and GHG concentrations (CO_2 = 276 ppm, CH_4 = 640 ppb, N_2O = 263 ppb) appropriate to 125 ka, but it was assumed that ice sheet configuration and land-sea geography is unchanged from modern and therefore no change was made to the isotopic composition of sea water. The LIG simulation is compared to a pre-industrial (PI) control with appropriate insolation, GHG and ice sheet forcing for 1850 CE.

150   There are GISS ModelE-R (LeGrande and Schmidt, 2009) simulations for eight time slices during the Holocene (9 ka, 6 ka, 5 ka, 4 ka, 3 ka, 2 ka, 1 ka and 0 ka). The 0 ka experiment is considered as the pre-industrial control (ca 1880). Orbital parameters were based on the Berger and Loutre (1991) solution and GHG concentrations were adjusted based on ice core reconstructions (Brook et al., 2000; Indermühle et al., 1999; Sowers, 2003) for each time slice. A remnant Laurentide ice sheet was included in the 9 ka simulation, following Licciardi et al. (1998), and the corresponding adjustment was made to mean ocean salinity

155   and ocean water $\delta^{18}O$ to account for this (Carlson et al., 2008). The ice sheet in all the other experiments was specified to be the same as modern, and therefore no adjustment was necessary. The simulations were run using the M20 version of GISS ModelE-R, which has a horizontal resolution of 4° by 5°. Each experiment was run for 500 years and we use the last 100 simulated years for the analyses.

2.3 Principle Coordinate Analysis and Redundancy Analysis

160   We used Principle Coordinate Analysis (PCoA) to identify regionally coherent patterns in the speleothem $\delta^{18}O$ records for the Holocene. PCoA is a multivariate ordination technique that uses a distance/dissimilarity matrix to represent inter-object (dis)similarity in reduced space (Gower, 1966; Legendre and Legendre, 1998). Speleothem records from individual sites are often discontinuous; missing data is problematic for many ordination techniques. PCoA is more robust to missing data that other methods (Kärkkäinen and Saarela, 2015; Rohlf, 1972). We used a correlation matrix of speleothem records as the

165 (dis)similarity measure. The temporal resolution of speleothem records was first standardised by calculating a running average mean with non-overlapping 500-year windows. This procedure produces a single composite record when there are several records for a given site. We used the 'broken stick' model (Bennett, 1996) to identify which PCoA axes were significant. We used redundancy analysis (RDA: Legendre and Legendre, 1998; Rao, 1964) with latitude and longitude as predictor variables to identify if PCoA (dis)similarities were related to geographical location, and Principal Components Analysis (PCA) to

170 identify the main patterns of variation. As these explanatory variables are not dimensionally homogeneous, they were centred on their means and standardised to allow direct comparison of the gradients. PCoA and RDA analyses were carried out using the 'vegan' package in R (Oksanen et al., 2019).

2.4 Glacial-interglacial changes in $\delta^{18}O$

We examined glacial-interglacial shifts in $^{18}O_{spel}$ and $\delta^{18}O_{precip}$ in regions influence by the monsoon, focusing on regional

175 differences between MH, LGM and LIG with respect to the present-day for speleothems or the control simulation experiment for model outputs. Comas-Bru et al. (2019) have shown that differences in speleothem $\delta^{18}O$ data between the 20th century and the pre-industrial period (i.e. 1850±15 CE) are within the temporal and measurement uncertainties of the data, and thus the use of different reference periods (i.e. PI for the ECHAM LIG experiment, 20th century for ECHAM MH, LGM experiments) should have little effect on our analyses. We used mean site $\delta^{18}O_{spel}$ values for each period for the regions identified in the

180 PCoA analysis. Where there are multiple speleothem $\delta^{18}O$ records for a site in a time period, they were averaged to calculate mean $\delta^{18}O_{spel}$. Three sites above 3500m were excluded from the calculation of the means because high elevation sites have more negative $\delta^{18}O$ values than their low-elevation counterparts and their inclusion would distort the regional estimates.

There are relatively few speleothems covering both the present-day and the period of interest (i.e., MH, LGM or LIG), precluding the calculation of $\delta^{18}O_{spel}$ anomalies from the speleothem data. We therefore calculated anomalies with respect to

185 modern (1960-2017 CE) using as reference a global gridded dataset of interpolated mean annual precipitation-weighted $\delta^{18}O_{precip}$ data (Bowen, 2018; Bowen and Revenaugh, 2003). This dataset combines data from 348 stations from the Global Network of Isotopes in Precipitation (IAEA/WMO, 2018), covering part or all of the period 1960-2014, and other records available at the Water Isotopes Database (Waterisotopes Database, 2017).

OIPC $\delta^{18}O_{precip}$ was converted to its speleothem equivalent assuming that: (i) precipitation-weighted mean annual $\delta^{18}O_{precip}$ is

190 equivalent to mean annual drip-water $\delta^{18}O$ (Yonge et al., 1985) and (ii) precipitation of calcite is consistent with the empirical speleothem-based kinetic fractionation factor of Tremaine et al. (2011) and precipitation of aragonite follows the fractionation factor from Grossman and Ku (1986), as formulated by Lachniet (2015):

$$\delta^{18}O_{calcite\_SMOW} = w\delta^{18}O_{precip\_SMOW} + \left(\left(\frac{16.1 \cdot 1000}{T}\right) - 24.6\right) \qquad \text{(T in K)} \qquad (1)$$

195
$$\delta^{18}O_{aragonite\_SMOW} = w\delta^{18}O_{precip\_SMOW} + \left(\left(\frac{18.34 \cdot 1000}{T}\right) - 31.954\right) \qquad \text{(T in K)} \qquad (2)$$

where $\delta^{18}O_{calcite\_SMOW}$ and $\delta^{18}O_{aragonite\_SMOW}$ are the speleothem isotopic composition for calcite and aragonite speleothems with reference to the V-SMOW standard (in permil); $w\delta^{18}O_{precip}$ is the OIPC precipitation-weighted annual mean isotopic composition of precipitation with respect to the V-SMOW standard and T is the mean annual cave temperature (in degrees Kelvin). We used the long-term (1960-2016) mean annual surface air temperature from the CRU-TS4.01 database (Harris et al., 2014) at each site as a surrogate for mean annual cave air temperature. The resolution of the gridded data means that $w\delta^{18}O_{precip\_SMOW}$ and T may be the same for nearby sites.

We use the V-SMOW to V-PDB conversion from Coplen et al. (1983), which is independent of speleothem mineralogy:

$$\delta^{18}O_{PDB} = 0.97001 \cdot \delta^{18}O_{SMOW} - 29.29 \qquad (3)$$

where $\delta^{18}O_{PDB}$ is relative to the V-PDB standard and $\delta^{18}O_{SMOW}$ is relative to V-SMOW standard.

Average uncertainties in the speleothem age models are ~50 years during the Holocene. This interval is smaller than the time windows used in this analysis, and age uncertainty is therefore expected to have a negligible impact on the results. We investigated the influence of age uncertainties on the LGM and LIG $\delta^{18}O_{spel}$ anomalies by examining the impact of using different window widths ($\pm$ 500, $\pm$ 700, $\pm$ 1000, $\pm$ 2000 years) on the regional mean $\delta^{18}O_{spel}$ anomalies.

We used anomalies of $w\delta^{18}O_{precip}$, mean annual surface air temperature (MAT) and mean annual precipitation (MAP) from the ECHAM5-wiso simulations to investigate the drivers of glacial-interglacial $\delta^{18}O_{spel}$ variability. Values were calculated from land grid cells (>50% land) $\pm3°$ around each speleothem site. This distance was chosen with reference to the coarsest resolution simulation (LIG, ca. 3.75 x 3.75°). Gridded values of MAT and MAP were weighted by the proportion of each grid cell that lies within $\pm3°$ of the site and linear distance-weighted means were calculated for each site and time slice. We only considered regions with at least one speleothem record for each of the three time periods, although these were not required to be the same sites, and where the observed shifts in $\delta^{18}O_{spel}$ were in the same direction and of a similar magnitude to the simulated $w\delta^{18}O_{precip}$.

2.5 Holocene and Last Interglacial regional trends

Speleothem $\delta^{18}O$ changes through the Holocene were examined by creating composite time-series for each region identified in the PCoA analysis with at least four Holocene records (> 5000 years long). Regional composites were constructed using a 4-step procedure, modified from Marlon et al. (2008): (i) the $\delta^{18}O$ data for individual speleothems were standardised to z-scores by subtracting the mean $\delta^{18}O_{spel}$ for a defined base period (7,000 to 3,000 years BP) then dividing these anomalies by the base period standard deviation. The base period was chosen to maximise the number of records included in each composite; (ii) the standardised data for a site were re-sampled by applying a 100-year non-overlapping running mean with the first bin centred at 50 years BP, in order to create a single site time series while ensuring that highly resolved records do not dominate the regional composite; (iii) each regional composite was constructed using locally weighted regression (Cleveland and Devlin, 1988) with a window width of 3,000 years and fixed target points in time; and (iv) confidence intervals (5th and 95th percentiles) for each composite were generated by bootstrap resampling by site over 1,000 iterations. There are too few sites to construct regional composites for the LIG and thus the trends in $\delta^{18}O_{spel}$ were examined using records from individual sites covering the period 130-116 ka BP.

We calculated Holocene regional composites from simulated $\delta^{18}O_{precip}$ from the GISS model. Simulated $\delta^{18}O_{precip}$ trends were

230   calculated using linear distance-weighted mean $\delta^{18}O_{precip}$ values from land grid cells (>50% land) within ±4° around each site. This distance was determined by the grid resolution of the model. Regional composites were then produced using bootstrap resampling in the same way as for the speleothem data. The simulated anomalies are relative to the control run rather than the specified base period used for the speleothem-based composites, so absolute values of simulated and observed Holocene trends are expected to differ. Preliminary analyses showed that neither the mean values nor trends in $\delta^{18}O_{precip}$ were substantially

235   different if the sampled area was reduced to match the sampling used for the ECHAM-based box plot analysis, or was increased to encompass the larger regions shown in Fig. 1 and used in the multiple regression analysis.

2.6 Multiple regression analysis

We investigate the drivers of regional $\delta^{18}O_{precip}$, and by extension $\delta^{18}O_{spel}$, through the Holocene using multiple linear regression (MLR) of simulated $\delta^{18}O_{precip}$ and climate variables chosen to represent the four potential large-scale drivers of

240   regional changes in the speleothem $\delta^{18}O$ records. Specifically, we use changes in mean precipitation and precipitation recycling over the monsoon regions, and changes in mean surface air temperature and surface wind direction over the moisture source regions. Whereas the influence of changes in precipitation, recycling and temperature are relatively direct measures, the change in surface wind direction over the moisture source region is used as an index of potential changes in the moisture source region and transport pathway. The boundaries of each monsoon region (Fig. 1) were defined to include all the speleothem sites used

245   to construct the Holocene $\delta^{18}O_{spel}$ composites. Moisture source area limits (Fig. 1) were defined based on moisture tracking studies (Bin et al., 2013; Breitenbach et al., 2010; D'Abreton and Tyson, 1996; Drumond et al., 2008, 2010; Durán-Quesada et al., 2010; Kennett et al., 2012; Nivet et al., 2018; Wurtzel et al., 2018) and GISS simulated summer surface winds. All climate variables were extracted for the summer months, defined as May to September (MJJAS) for northern hemisphere regions and November to March (NDJFM) for southern hemisphere regions (Wang and Ding, 2008). Only grid cells with

250   >50% land were used to extract variables over monsoon regions and only grid cells with <50% land were used to extract variables over moisture source regions. The inputs to the MLR for each time interval were calculated as anomalies from the control run.

Precipitation recycling was calculated as the ratio of locally sourced precipitation versus total precipitation. Although the GISS E-R mid-Holocene experiment explicitly estimates recycling using vapour source distribution tracers (Lewis et al., 2014), this

255   was not done for all the Holocene time slice simulations. Therefore, we calculate a precipitation recycling index (RI), following Brubaker et al. (1993):

$$RI \;=\; \frac{P_R}{P} = \frac{E}{2Q_H + E} \tag{3}$$

Where locally sourced (recycled) precipitation (P_R) is estimated using total evaporation over a region (E) and total precipitation (P) is estimated as the sum of total evaporation and net incoming moisture flux integrated across the boundaries of the region

260 (Q_H). RI therefore expresses the change in the contribution of local, recycled precipitation independently of any overall change in precipitation amount.

We use pseudo-R^2 to determine the goodness-of-fit for the overall MLR model, and t values (the regression coefficient divided by its standard error) to determine the strength of each relationship. Partial residual plots were used to show the relationship between each predictor variable and $\delta^{18}O_{precip}$ when the effects of the other variables are removed.

265 All statistical analyses were performed in R (R Core Team, 2019) and plots were generated using ggplot (Wickham, 2016).

3 Results

3.1 Principle Coordinate Analysis and Redundancy Analysis

The first two PCoA axes are significant, according to the broken stick test, and account for 65% and 20% of $\delta^{18}O_{spel}$ variability respectively (Table 1). The PCoA scores differentiate records geographically (Fig. 2a): southern hemisphere monsoon regions such as the southwestern South American Monsoon (SW-SAM) and South African Monsoon (SAfM) are characterised by

270 consistently low PCoA1 scores over time, whilst northern hemisphere monsoons such as the Indian Summer Monsoon (ISM) and the East Asian Monsoon (EAM), are characterised by higher PCoA1 scores. Most southern hemisphere regions also have lower PCoA2 scores although this is not consistent over time. Speleothem records from Central America (CAM) and Indonesian-Australian monsoon (IAM) have PCoA scores intermediate between the northern and southern hemisphere regions. PCoA clearly separates the South American records into a northeastern region (NE-SAM) with scores similar to other northern

275 hemisphere monsoon regions and a southwestern region (SW-SAM), with scores similar to other southern hemisphere regions. The RDA supports a geographical control on the (dis)similarity of speleothem $\delta^{18}O$ records over the Holocene (Fig. 2b). RDA1 explains 37% of the variability and is significantly correlated with both latitude and longitude (Table 2).

3.2 Regional interglacial-glacial differences

280 Only the ISM, EAM and IAM regions have sufficient data (i.e. at least one record from every time period) to allow comparisons across the MH, LGM and LIG (Fig. 3) and have similar shifts in observed $\delta^{18}O_{spel}$ and simulated $\delta^{18}O_{precip}$. The regional mean $\delta^{18}O_{spel}$ anomalies calculated for different time windows (± 500, ± 700, ± 1000, ± 2000 years) vary by less than 0.35‰ for the LGM (ISM: <0.16‰, EAM: <0.35‰, IAM: <0.22‰) and 0.48 ‰ for the LIG (ISM: <0.16‰, EAM: <0.48‰, IAM: <0.11‰), indicating that age uncertainties have a minimal impact on these mean values. The most positive $\delta^{18}O_{spel}$ anomalies in all three

285 regions occur at the LGM, with more negative anomalies for the MH and LIG. The simulated $\delta^{18}O_{precip}$ anomalies show a similar pattern, more positive anomalies during the LGM than during the MH or the LIG. Although the mean values of the simulated $\delta^{18}O_{precip}$ anomalies differ from the observed $\delta^{18}O_{spel}$ anomalies, they are consistent with the observations within the range of their uncertainties. The differences in regional $\delta^{18}O_{spel}$ anomalies between MH and LIG differ across the three regions. In both the ISM and the EAM, differences in $\delta^{18}O_{spel}$ values between the MH and LIG are small (Fig. 3a,b), although ISM LIG

290 $\delta^{18}O_{spel}$ values are slightly more negative than MH values. In the IAM, MH values are less negative than the LIG (Fig. 3c).

However, there are only a limited number of speleothem records from the ISM and IAM during the LIG, so the apparent differences between the two intervals in these regions may not be meaningful. The glacial-interglacial changes in $\delta^{18}O_{precip}$ are consistent with the simulated temperature and precipitation changes, with warmer and wetter conditions during interglacials and cooler and drier conditions during the LGM in all three regions. Differences in simulated precipitation between the MH and the LIG could help explain the differences between $\delta^{18}O_{spel}$ in the ISM and IAM, since the LIG is wetter than the MH in the ISM and drier than the MH in the IAM. However, the LIG is also drier than the MH in the EAM, a feature that appears inconsistent with the lack of differentiation between the $\delta^{18}O$ signals in this region.

3.3 Regional-scale interglacial $\delta^{18}O$ evolution

There are four regions with sufficient data to examine Holocene trends: EAM, ISM, SW-SAM and IAM (Fig. 4). The IAM region has the fewest records (n=7) whilst the EAM has the largest number (n=14). The regional composites are z-scores, i.e. anomalies with respect to the base period (3000-7000 yr BP). The confidence intervals on the regional composites are small for all regions, except SW-SAM in the early Holocene. The EAM and ISM regions (Fig. 4 left) show the most positive $\delta^{18}O_{spel}$ z-scores around 12 ka followed by a rapid decrease towards their most negative values at ~9.5 ka and ~9 ka, respectively. The $\delta^{18}O_{spel}$ z-scores in the EAM are relatively constant from 9.5 to ~7 ka, whereas this plateau is present but less marked in the ISM. There is a gradual trend towards more positive $\delta^{18}O_{spel}$ z-scores towards the present in both regions thereafter. The SW-SAM records (Fig. 4i) have their most positive $\delta^{18}O_{spel}$ z-scores in the early Holocene with a gradual trend to more negative scores towards the present. By contrast, the IAM z-scores (Fig. 4g) are most positive at 12ka, gradually decreasing until ca 5 ka and are relatively flat thereafter.

There are insufficient data to create composite curves for the LIG, but individual records from the four regions (Fig. 5) show similar features to the Holocene trends. Records from the ISM and EAM (Fig. 5 left), for example, are characterised by an initial sharp decrease in $\delta^{18}O_{spel}$ values of about 4 ‰ between 130-129 ka and then most of the records (Dykoski et al., 2005; Kathayat et al., 2016; Wang et al., 2008) show little variability for several thousand years. Despite the fact that the Tianmen record (Cai et al., 2010, 2012) shows considerable variability between 123-127 ka, there is nevertheless a similar plateau in the average observed value before the rapid change to less negative values after 127 ka. Similar to the Holocene, the SW-SAM record (Cheng et al., 2013) shows increasingly negative $\delta^{18}O_{spel}$ values through the LIG. The trend shown for Whiterock cave (Carolin et al., 2016) also shows similar features to the IAM Holocene composite, with a gradual trend towards more negative values initially and a relatively complacent curve towards the end of the interglacial (Fig. 5 right).

3.4 Multiple regression analysis of Holocene $\delta^{18}O_{precip}$

The global multiple linear regression model that includes all of the Holocene (1 to 9ka) $\delta^{18}O_{precip}$ regional trends has a pseudo-R^2 of 0.80 and shows statistically significant relationships between the anomalies in $\delta^{18}O_{precip}$ and anomalies in precipitation amount, temperature and surface wind direction (Table 3). There is a strong negative relationship with precipitation amount (t value = -8.75) and a strong positive relationship (t value = 8.03) with surface wind direction over the moisture source region,

an index of changes in either source area or moisture pathway. The relationship with temperature over the moisture source region is weaker, but positive (t value = 2.05). Precipitation recycling is not significant in this global analysis.

325 There are too few data points to make regressions for individual monsoon regions, but the distribution of data points for each region in the partial residual plots (Fig. 6) is indicative of the degree of conformity to the global model. Data points from the ISM, SW-SAM, IAM and SAfM are well aligned with the global relationship with precipitation amount (Fig. 6a), indicating that precipitation amount is an important control on changes in $\delta^{18}O_{precip}$ in these regions. The NE-SAM, EAM and CAM values deviate somewhat from the global relationship and, although there are relatively few points, this suggests that changes

330 in precipitation are a less important influence on $\delta^{18}O_{precip}$ changes in these regions. The impact of temperature changes (Fig. 6b) in the ISM, EAM and SW-SAM is broadly consistent with the global model. The slope of the relationship with temperature is negative for the IAM and NE-SAM, and since this is physically implausible it suggests that some factor not currently included in the MLR is influencing these records. However, the inconsistencies between the regional signals helps to explain why the global relationship between anomalies in temperature and $\delta^{18}O_{precip}$ is weak (Fig. 6b) and probably reflects the fact

335 that tropical temperature changes during the Holocene are small. Data points from the EAM, ISM and IAM are well aligned with the global relationship between changes in $\delta^{18}O_{precip}$ and changes in wind direction (Fig. 6c), indicating that changes in source area or moisture pathway are an important control on changes in $\delta^{18}O_{precip}$ in these regions. However, values for CAM, SW-SAM, NE-SAM and SAfM deviate strongly from the global relationship. Recycling does not appear to be an important contributor to changes in $\delta^{18}O_{precip}$ except in SW-SAM and SAfM (Fig. 6d).

340 **4 Discussion**

We have shown that it is possible to derive an objective regionalisation of speleothem records based on PCoA of the oxygen-isotope trends through the Holocene (Fig. 2). This approach separates out regions with a distinctive northern hemisphere signal (e.g. ISM, EAM, NE-SAM) from regions with a distinctive southern hemisphere signal (e.g. SW-SAM, SAfM), reflecting the fact that the evolution of regional monsoons in each hemisphere follows, to some extent, insolation forcing. It also identifies

345 regions that have an intermediate pattern (e.g. IAM). The robustness of the regionalisation is borne out by the fact that Holocene composite trends from each region have tight confidence intervals (Fig. 4), showing that the signals of individual records across a region show broad similarities. The monsoon regions identified by PCoA are consistent with previous studies (Wang et al., 2014). The tracking of northern hemisphere insolation is a recognised feature of monsoon systems in India and China (see reviews by Kaushal et al., 2018; Zhang et al., 2019). The separation of speleothem records from NE-SAM from those in

350 SW-SAM is consistent with the precipitation dipole that exists between northeastern Brazil (Nordeste) and the continental interior (Berbery and Barros, 2002; Boers et al., 2014). The anti-phasing of speleothem records from the two regions during the Holocene has been recognised in previous studies (Cruz et al., 2009; Deininger et al., 2019). The intermediate nature of the records from the maritime continent is consistent with the fact that the Indonesian-Australian (IAM) summer monsoon is influenced by cross-equatorial air flow and hence can be influenced by northern hemisphere conditions (Trenberth et al., 2000).

355   Palaeoenvironmental records from this region show mixed signals for the Holocene: some have been interpreted as showing enhanced (Beaufort et al., 2010; Mohtadi et al., 2011; Quigley et al., 2010; Wyrwoll and Miller, 2001) and others reduced precipitation (Kuhnt et al., 2015; Steinke et al., 2014) during the early and mid-Holocene. Modelling studies have shown that this region is highly sensitive to SST changes in the Indian Ocean and southern China Sea, which in turn reflect changes in the northern hemisphere winter monsoons. Although most climate models produce a reduction in precipitation across the IAM

360   during the mid-Holocene in response to orbital forcing, this is less than might be expected in the absence of ocean feedbacks associated with changes in the Indian Ocean (Zhao and Harrison, 2012).

    The separation of northern and southern monsoon regions is consistent with the idea that changes in monsoon rainfall are primarily driven by changes in insolation (Ding and Chan, 2005; Kutzbach et al., 2008). Indeed, regional $\delta^{18}O_{spel}$ composites from the EAM, ISM and SW-SAM show a clear relationship with the long-term trends in local summer insolation (Fig. 4).

365   Similar patterns are seen in individual speleothem records from each region confirming that the composite trends are representative. However, the composite trends are not an exact mirror of the insolation signal over the Holocene. For example, the ISM and EAM composites show a more rapid rise during the early Holocene than implied by the insolation forcing. The maximum wet phase in these two regions lasts for ca 3,000 years, again contrasting with the gradual decline in insolation forcing after its peak at ca 11 ka. Both the rapid increase and the persistence of wet conditions for several thousand years is

370   also observed in other palaeohydrological records across southern and central China, including pollen (Zhao et al., 2009; Li et al., 2018) and peat records (Hong et al., 2003; Zhou et al., 2004). These features are also characteristic of lake records from India (Misra et al., 2019). The lagged response to increasing insolation is thought to be due to the presence of northern hemisphere ice sheets in the early Holocene (Zhang et al., 2018). The persistence of wetter conditions through the early and mid-Holocene is thought to reflect the importance of land-surface and ocean feedbacks in sustaining regional monsoons

375   (Dallmeyer et al., 2010; Kutzbach et al., 1996; Marzin and Braconnot, 2009; Rachmayani et al., 2015; Zhao and Harrison, 2012). We have shown that there is little difference in the isotopic values between the MH and the LIG in the ISM and EAM regions, which is also observed in individual speleothem records (Kathayat et al., 2016; Wang et al., 2008). Given that the increase in summer insolation is much larger during the LIG than the MH, this finding is again consistent with the idea that other factors play a role in modulating the monsoon response to insolation forcing.

380   Global relationships between $\delta^{18}O_{precip}$ and its drivers (precipitation amount, temperature and surface wind direction; Fig. 6) are consistent with existing studies: a strong relationship with precipitation and a weaker temperature effect has been widely observed at tropical and sub-tropical latitudes in modern observations (Dansgaard, 1964; Rozanski et al., 1993). The significant global relationship between $\delta^{18}O_{precip}$ and surface winds supports the idea that changes in moisture source and pathway are also important for explaining $\delta^{18}O$ variability over the Holocene. The multiple regression analysis also provides insights into the

385   relative importance of different influences at a regional scale. In the ISM, the results support existing speleothem studies that suggest changes in precipitation amount (Cai et al., 2015; Fleitmann et al., 2004) and to a lesser extent moisture pathway (Breitenbach et al., 2010) drive $\delta^{18}O_{spel}$ variability. The $\delta^{18}O$ variability in the IAM region through the Holocene also appears to be strongly driven by changes in precipitation and moisture pathway, consistent with the interpretation of Wurtzel et al.

(2018). Changes in precipitation amount do not seem to explain the observed changes in $\delta^{18}O_{spel}$ in the EAM during the

390   Holocene, where Holocene $\delta^{18}O_{precip}$ evolution is largely driven by changes in atmospheric circulation (indexed by changes in surface winds). This is consistent with existing studies that emphasise changes in moisture source and/or pathway rather than a precipitation amount (Maher, 2016; Maher and Thompson, 2012; Tan, 2014; Yang et al., 2014). Speleothem $\delta^{18}O$ records in the SW-SAM clearly reflect regional-scale changes in precipitation, consistent with interpretations of individual records (Cruz et al., 2009; Kanner et al., 2013). However, this is a region where changes in precipitation recycling also appears to be

395   important, perhaps unsurprisingly given that recycling presently contributes ca 25-35% of the precipitation over the Amazon (Brubaker et al., 1993; Eltahir and Bras, 1994).

The LGM is characterised by a similar orbital configuration to today, however global ice volume was at a maximum and GHG concentrations were lower than present. The $\delta^{18}O_{spel}$ anomalies are more positive during the LGM than the MH or LIG, suggesting drier conditions in the ISM, EAM and IAM, supported by simulated changes in $\delta^{18}O_{precip}$ and precipitation (Fig. 3).

400   Cooler SSTs of approximately 2°C (relative to the MH and LIG) in the ISM and EAM and of approximately 3°C in IAM source areas, together with a ca 5% decrease in relative humidity (Yue et al., 2011) would result in a water vapour $\delta^{18}O$ signal at the source ca 1 ‰ more depleted than seawater. This depletion results from the temperature dependence of equilibrium fractionation during evaporation and kinetic isotope effects related to humidity (Clark and Fritz, 1997). This fractionation counteracts any impact from enriched seawater $\delta^{18}O$ values during the LGM (ca. +1 ‰ relative to the MH or LIG; Waelbroeck

405   et al., 2002). Enriched $\delta^{18}O_{precip}$ and $\delta^{18}O_{spel}$ values during the LGM must therefore be caused by a significant decrease in atmospheric moisture and precipitation.

We have used version 2 of the SISAL database (Atsawawaranunt et al., 2018; Comas-Bru et al., 2020a) in our analyses. Despite the fact that SISALv2 includes more than 70% of known speleothem isotope records, there are still too few records from some regions (e.g. Africa, the Caribbean) to make meaningful analyses. The records for older time periods are also sparse. There are

410   only 14 records from monsoon regions covering the LIG in SISALv2, for example. Nevertheless, our analyses show that there are robust and explicable patterns for most monsoon regions during the Holocene and sufficient records to make meaningful analyses of the LGM and LIG. Whilst there is a need for the generation of new speleothem records from key regions such as northern Africa, further expansion of the SISAL database will certainly provide additional opportunities to analyse the evolution of the monsoons through time.

415   The impact of age uncertainties, included in SISALv2, are not taken into account in our analyses. Age uncertainties during the Holocene are smaller than the interval used for binning records and the width of the time windows used, and thus should not have a significant effect on our conclusions. The mean age uncertainty at the LGM and LIG is ca 430 and 1140 years, respectively. However, varying the window length for the selection of LGM and LIG samples from ±500 to ±2000 years, thereby encompassing this uncertainty, has a negligible effect (<0.5 ‰) on the average $\delta^{18}O$ values. Thus, the interglacial-

420   glacial contrast in regional $\delta^{18}O_{spel}$ is also robust to age uncertainties.

Isotope-enabled climate models are used in this study to explain observed regional-scale trends in $\delta^{18}O_{spel}$. There is a limited number of isotope-enabled models, and there are no simulations of the same time period using the same experimental protocol.

Although there are simulations of the MH from both ECHAM5-wiso and GISS, for example, these models have different grid resolutions and used different boundary conditions. This could help to explain why the two models yield different estimates

425 of the change in regional $\delta^{18}O_{precip}$ (of 0.5 ‰) at the MH. However, both models show trends in $\delta^{18}O_{precip}$ that reproduce the observed changes in regional $\delta^{18}O_{spel}$ (Figs 3 and 4), and this provides a basis for using these models to explore the causes of these trends on different timescales. The failure to reproduce the LGM $\delta^{18}O_{spel}$ signal in SW-SAM in the ECHAM5-wiso model, which precluded a consideration of interglacial-glacial shifts in this region, is a common feature of other isotope-enabled simulations (Caley et al., 2014; Risi et al., 2010).

430 This study illustrates a novel data-model approach to investigate the drivers of $\delta^{18}O_{spel}$ under past conditions, by comparing composite regional records and then using multiple linear regression of isotope-enabled palaeoclimate simulations to determine the role of individual drivers of these trends. This obviates the need to use modern $\delta^{18}O_{precip}$-climate relationships to explain changes under conditions considerably different from today or to rely on coherency between different palaeohydrological archives which may respond to different climate variables. This model interrogation approach could be employed to address

435 questions about the regional drivers of speleothem records outside the monsoon regions.

5 Conclusions

Geographically distributed speleothem $\delta^{18}O$ records and isotope-enabled climate models can be used together to understand the drivers of $\delta^{18}O_{spel}$ on orbital timescales. Speleothem records, objectively grouped into monsoon regions by record correlation and multivariate ordination techniques, show regional trends that are consistent with changes in summer insolation

440 but modulated by land-surface and ocean feedbacks Glacial $\delta^{18}O_{spel}$ signals are best explained by a large decrease in precipitation, as a consequence of lower atmospheric moisture content driven by global cooling. The evolution of $\delta^{18}O_{spel}$ through the Holocene across the global monsoon domain is driven by changes in precipitation, atmospheric circulation and temperature. At the regional scale, our analyses support the increasing number of studies suggesting that East Asian monsoon speleothem $\delta^{18}O$ evolution through the Holocene relates to changes in atmospheric circulation (i.e. changes in moisture

445 pathway and/or source). Changes in precipitation amount are the predominant driver of Holocene $\delta^{18}O_{spel}$ evolution in the Indian, southwestern South American and Indonesian-Australian monsoons, although changes in atmospheric circulation also contribute in the Indian and Indonesian-Australian monsoon regions and changes in precipitation recycling in southwestern South America.

450 **Code and data availability**

The SISAL (Speleothem Isotopes Synthesis and AnaLysis) database version 2 is available through the University of Reading Research Archive at http://dx.doi.org/10.17864/1947.242. The ECHAM5-wiso MH and LGM simulations are available at

https://doi.org/10.1594/PANGAEA.902347. The ECHAM LIG simulation is available at https://doi.pangaea.de/10.1594/PANGAEA.879229. The OIPC mean annual $\delta^{18}O_{precip}$ data are available at

455   http://wateriso.utah.edu/waterisotopes/pages/data_access/ArcGrids.html. CRU-TS4.01 mean annual temperature data are available at http://doi.org/10/gcmcz3. The code used to generate the figures in this paper is available at https://doi.org/10.5281/zenodo.3875496.

Author contributions

The study was designed by SP, SPH, LCB and NK. MW and ALG provided climate model outputs. SP ran the analyses. The
460   first draft of the manuscript was written by SP, SPH and LCB and all authors contributed to the final draft.

Competing interests

The authors declare no competing interests.

Funding

SP, LCB and SPH acknowledge funding support from the ERC-funded project GC2.0 (Global Change 2.0: Unlocking the past
465   for a clearer future, grant number 694481). SPH also acknowledges support from the JPI-Belmont Forum project "Palaeoclimate Constraints on Monsoon Evolution and Dynamics (PaCMEDy)" funded through NERC (NE/P006752/1).

Acknowledgements

Ideas in this paper were developed at a meeting of the SISAL (Speleothem Isotopes Synthesis and Analysis) working group of the Past Global Changes (PAGES) programme. We thank PAGES for their support for this meeting and our colleagues in
470   SISAL for the useful discussions. We thank Gabriele Messori for help with the code for calculating precipitation recycling.

References

Aggarwal, P. K., Alduchov, O. A., Froehlich, K. O., Araguas-Araguas, L. J., Sturchio, N. C. and Kurita, N.: Stable isotopes in
475   global precipitation: A unified interpretation based on atmospheric moisture residence time, Geophys. Res. Lett., 39(11), https://doi.org/10.1029/2012GL051937, 2012.

Atsawawaranunt, K., Comas-Bru, L., Amirnezhad Mozhdehi, S., Deininger, M., Harrison, S. P., Baker, A., Boyd, M., Kaushal,

N., Masood Ahmad, S., Ait Brahim, Y., Arienzo, M., Bajo, P., Braun, K., Burstyn, Y., Chawchai, S., Duan, W., Hatvani, I.
G., Hu, J., Kern, Z., Labuhn, I., Lachniet, M., Lechleitner, F. A., Lorrey, A., Pérez-Mejías, C., Pickering, R., Scroxton, N. and
480 SISAL working group members: The SISAL database: A global resource to document oxygen and carbon isotope records from
speleothems, Earth Syst. Sci. Data, 10, 1687–1713, https://doi.org/10.5194/essd-10-1687-2018, 2018.

Bailey, A., Posmentier, E. and Feng, X.: Patterns of evaporation and precipitation drive global isotopic changes in atmospheric
moisture, Geophys. Res. Lett., 45(14), https://doi.org/10.1029/2018GL078254, 2018.

Bar-Matthews, M., Ayalon, A. and Kaufman, A.: Late Quaternary paleoclimate in the eastern Mediterranean region from stable
485 isotope analysis of speleothems at Soreq Cave, Israel, Quat. Res., 47(2), 155–168, https://doi.org/10.1006/qres.1997.1883,
1997.

Battisti, D. S., Ding, Q. and Roe, G. H.: Coherent pan-Asian climatic and isotopic response to orbital forcing of tropical
insolation, J. Geophys. Res. Atmos., 119(21), 11997-12020, https://doi.org/ 10.1002/2014JD021960, 2014.

Beaufort, L., Van Der Kaars, S., Bassinot, F. C. and Moron, V.: Past dynamics of the Australian monsoon: precession, phase
490 and links to the global monsoon concept, Clim. Past, 6, 695–706, https://doi.org/10.5194/cp-6-695-2010, 2010.

Bennett, K. D.: Determination of the number of zones in a biostratigraphical sequence, New Phytol., 132(1), 155–170,
https://doi.org/10.1111/j.1469-8137.1996.tb04521.x, 1996.

Berbery, E. H. and Barros, V. R.: The hydrologic cycle of the La Plata basin in South America, J. Hydrometeorol., 3(6), 630–
645, https://doi.org/10.1175/1525-7541(2002)003<0630:THCOTL>2.0.CO;2, 2002.

495 Berger, A. and Loutre, M. F.: Insolation values for the climate of the last 10 million years, Quat. Sci. Rev., 10(4), 297–317,
https://doi.org/10.1016/0277-3791(91)90033-Q, 1991.

Berger, A. L.: Long-term variations of daily insolation and Quaternary climatic changes, J. Atmos. Sci., 35(12), 2362–2367,
https://doi.org/10.1175/1520-0469(1978)035<2362:ltvodi>2.0.co;2, 1978.

Bin, C., Xiang-De, X. and Tianliang, Z.: Main moisture sources affecting lower Yangtze River Basin in boreal summers during
500 2004-2009, Int. J. Climatol., 33(4), 1035–1046, https://doi.org/10.1002/joc.3495, 2013.

Boers, N., Rheinwalt, A., Bookhagen, B., Barbosa, H. M. J., Marwan, N., Marengo, J. and Kurths, J.: The South American
rainfall dipole: A complex network analysis of extreme events, Geophys. Res. Lett., 41(20), 7397–7405,
https://doi.org/10.1002/2014GL061829, 2014.

Bowen, G.: Gridded maps of the isotopic composition of meteoric waters, [online] Available from: http://waterisotopes.org
505 (Accessed 15 October 2018), 2018.

Bowen, G. J. and Revenaugh, J.: Interpolating the isotopic composition of modern meteoric precipitation, Water Resour. Res.,
39(10), https://doi.org/10.1029/2003WR002086, 2003.

Breitenbach, S. F. M., Adkins, J. F., Meyer, H., Marwan, N., Kumar, K. K. and Haug, G. H.: Strong influence of water vapor
source dynamics on stable isotopes in precipitation observed in Southern Meghalaya, NE India, Earth Planet. Sci. Lett., 292(1–
510 2), 212–220, https://doi.org/10.1016/j.epsl.2010.01.038, 2010.

Brook, E. J., Harder, S., Severinghaus, J., Steig, E. J. and Sucher, C. M.: On the origin and timing of rapid changes in
atmospheric methane during the Last Glacial Period, Global Biogeochem. Cycles, 14(2), 559–572,
https://doi.org/10.1029/1999GB001182, 2000.

Brubaker, K. L., Entekhabi, D. and Eagleson, P. S.: Estimation of continental precipitation recycling, J. Clim., 6(6), 1077–
1089, https://doi.org/10.1175/1520-0442(1993)006<1077:EOCPR>2.0.CO;2, 1993.

Cai, Y., Cheng, H., An, Z., Lawrence Edwards, R., Wang, X., Tan, L. and Wang, J.: Large variations of oxygen isotopes in precipitation over south-central Tibet during Marine Isotope Stage 5, Geology, 38(3), 243–246, https://doi.org/10.1130/G30306.1, 2010.

Cai, Y., Zhang, H., Cheng, H., An, Z., Lawrence Edwards, R., Wang, X., Tan, L., Liang, F., Wang, J. and Kelly, M.: The Holocene Indian monsoon variability over the southern Tibetan Plateau and its teleconnections, Earth Planet. Sci. Lett., 335, 135–144, https://doi.org/10.1016/j.epsl.2012.04.035, 2012.

Cai, Y., Fung, I. Y., Edwards, R. L., An, Z., Cheng, H., Lee, J. E., Tan, L., Shen, C. C., Wang, X., Day, J. A., Zhou, W., Kelly, M. J. and Chiang, J. C. H.: Variability of stalagmite-inferred Indian monsoon precipitation over the past 252,000 y, Proc. Natl. Acad. Sci. U. S. A., 112(10), 2954–2959, https://doi.org/10.1073/pnas.1424035112, 2015.

Caley, T., Roche, D. M., Waelbroeck, C. and Michel, E.: Oxygen stable isotopes during the Last Glacial Maximum climate: Perspectives from data-model (iLOVECLIM) comparison, Clim. Past, 10(6), 1939–1955, https://doi.org/10.5194/cp-10-1939-2014, 2014.

Carlson, A. E., LeGrande, A. N., Oppo, D. W., Came, R. E., Schmidt, G. A., Anslow, F. S., Licciardi, J. M. and Obbink, E. A.: Rapid early Holocene deglaciation of the Laurentide ice sheet, Nature Geosci., 1(9), 620-624, https://doi.org/10.1038/ngeo285, 2008.

Carolin, S. A., Cobb, K. M., Lynch-Stieglitz, J., Moerman, J. W., Partin, J. W., Lejau, S., Malang, J., Clark, B., Tuen, A. A. and Adkins, J. F.: Northern Borneo stalagmite records reveal West Pacific hydroclimate across MIS 5 and 6, Earth Planet. Sci. Lett., 439, 182–193, https://doi.org/10.1016/j.epsl.2016.01.028, 2016.

Chen, Z., Auler, A. S., Bakalowicz, M., Drew, D., Griger, F., Hartmann, J., Jiang, G., Moosdorf, N., Richts, A., Stevanovic, Z., Veni, G. and Goldscheider, N.: The World Karst Aquifer Mapping project: concept, mapping procedure and map of Europe, Hydrogeol. J., 25(3), 771–785, https://doi.org/10.1007/s10040-016-1519-3, 2017.

Cheng, H., Edwards, R. L., Wang, Y., Kong, X., Ming, Y., Kelly, M. J., Wang, X., Gallup, C. D. and Liu, W.: A penultimate glacial monsoon record from Hulu Cave and two-phase glacial terminations, Geology, 34(3), 217–220, https://doi.org/10.1130/G22289.1, 2006.

Cheng, H., Fleitmann, D., Edwards, R. L., Wang, X., Cruz, F. W., Auler, A. S., Mangini, A., Wang, Y., Kong, X., Burns, S. J. and Matter, A.: Timing and structure of the 8.2 kyr B.P. event inferred from $\delta^{18}O$ records of stalagmites from China, Oman, and Brazil, Geology, 37(11), 1007–1010, https://doi.org/10.1130/G30126A.1, 2009.

Cheng, H., Sinha, A., Cruz, F. W., Wang, X., Edwards, R. L., d'Horta, F. M., Ribas, C. C., Vuille, M., Stott, L. D. and Auler, A. S.: Climate change patterns in Amazonia and biodiversity, Nat. Commun., 4(1), 1411, https://doi.org/10.1038/ncomms2415, 2013.

Clark, I. and Fritz, P.: Environmental Isotopes in Hydrology, Lewis Publishers, New York., 1997.

Cleveland, W. S. and Devlin, S. J.: Locally weighted regression: An approach to regression analysis by local fitting, J. Am. Stat. Assoc., 83(403), 596–610, https://doi.org/10.1080/01621459.1988.10478639, 1988.

Cole, J. E., Rind, D., Webb, R. S., Jouzel, J. and Healy, R.: Climatic controls on interannual variability of precipitation $\delta^{18}O$: Simulated influence of temperature, precipitation amount, and vapor source region, J. Geophys. Res. Atmos., 104(D12),

14223–14235, https://doi.org/10.1029/1999JD900182, 1999.

Comas-Bru, L., Harrison, S. P., Werner, M., Rehfeld, K., Scroxton, N. and Veiga-Pires, C.: Evaluating model outputs using integrated global speleothem records of climate change since the last glacial, Clim. Past., 15(4), 1557-1579, https://doi.org/10.5194/cp-15-1557-2019, 2019.

555   Comas-Bru, L., Atsawawaranunt, K., Harrison, S. P. and SISAL working group members: SISAL (Speleothem Isotopes Synthesis and AnaLysis Working group) database version 2.0, http://dx.doi.org/10.17864/1947.242, 2020a.

Comas-Bru, L., Rehfeld, K., Roesch, C., Amirnezhad-Mozhdehi, S., Harrison, S. P., Atsawawaranunt, K., Ahmad, S. M., Ait Brahim, Y., Baker, A., Bosomworth, M., Breitenbach, S. F., Burstyn, Y., Columbu, A., Deininger, M., Demény, A., Dixon, B., Fohlmeister, J., Hatvani, I. G., Hu, J., Kaushal, N., Kern, Z., Labuhn, I., Lechleitner, F. A., Lorrey, A., Martrat, B., Novello,
560   V. F., Oster, J., Pérez-Mejías, C., Scholz, D., Scroxton, N., Sinha, N., Ward, B. M., Warken, S., Zhang, H. and SISAL working group members: SISALv2: A comprehensive speleothem isotope database with multiple age-depth models, Earth Syst. Sci. Data Discuss., https://doi.org/10.5194/essd-2020-39, in review, 2020b.

Coplen, T. B., Kendall, C. and Hopple, J.: Comparison of stable isotope reference samples, Nature, 302(5905), 236–238, https://doi.org/10.1038/302236a0, 1983.

565   Cruz, F. W., Burns, S. J., Karmann, I., Sharp, W. D., Vuille, M., Cardoso, A. O., Ferrari, J. A., Silva Dias, P. L. and Viana, O.: Insolation-driven changes in atmospheric circulation over the past 116,000 years in subtropical Brazil, Nature, 434(7029), 63–66, https://doi.org/10.1038/nature03365, 2005.

Cruz, F. W., Vuille, M., Burns, S. J., Wang, X., Cheng, H., Werner, M., Lawrence Edwards, R., Karmann, I., Auler, A. S. and Nguyen, H.: Orbitally driven east-west antiphasing of South American precipitation, Nat. Geosci., 2(3), 210–214,
570   https://doi.org/10.1038/ngeo444, 2009.

D'Abreton, P. C. and Tyson, P. D.: Three-dimensional kinematic trajectory modelling of water vapour transport over Southern Africa, Water SA, 22(4), 297–306, 1996.

Dallmeyer, A., Claussen, M. and Otto, J.: Contribution of oceanic and vegetation feedbacks to Holocene climate change in monsoonal Asia, Clim. Past, 6(2), 195–218, https://doi.org/10.5194/cp-6-195-2010, 2010.

575   Dansgaard, W.: Stable isotopes in precipitation, Tellus, 16(4), 436–468, https://doi.org/10.3402/tellusa.v16i4.8993, 1964.

Deininger, M., Ward, B. M., Novello, V. F. and Cruz, F. W.: Late Quaternary variations in the South American monsoon system as inferred by speleothems—New perspectives using the SISAL database, Quaternary, 2(1), 6, https://doi.org/10.3390/quat2010006, 2019.

Ding, Y. and Chan, J. C. L.: The East Asian summer monsoon: an overview, Meteorol. Atmos. Phys., 89(1–4), 117–142,
580   https://doi.org/10.1007/s00703-005-0125-z, 2005.

Dong, J., Wang, Y., Cheng, H., Hardt, B., Lawrence Edwards, R., Kong, X., Wu, J., Chen, S., Liu, D., Jiang, X. and Zhao, K.: A high-resolution stalagmite record of the Holocene East Asian monsoon from Mt Shennongjia, central China, Holocene, 20(2), 257–264, https://doi.org/10.1177/0959683609350393, 2010.

Drumond, A., Nieto, R., Gimeno, L. and Ambrizzi, T.: A Lagrangian identification of major sources of moisture over Central
585   Brazil and la Plata Basin, J. Geophys. Res. Atmos., 113(D14), https://doi.org/10.1029/2007JD009547, 2008.

Drumond, A., Nieto, R., Trigo, R., Ambrizzi, T., Souza, E. and Gimeno, L.: A Lagrangian identification of the main sources

of moisture affecting northeastern Brazil during its pre-rainy and rainy seasons, PLoS One, 5(6), https://doi.org/10.1371/journal.pone.0011205, 2010.

590 Durán-Quesada, A. M., Gimeno, L., Amador, J. A. and Nieto, R.: Moisture sources for Central America: Identification of moisture sources using a Lagrangian analysis technique, J. Geophys. Res. Atmos., 115(5), 1–15, https://doi.org/10.1029/2009JD012455, 2010.

Dykoski, C. A., Edwards, R. L., Cheng, H., Yuan, D., Cai, Y., Zhang, M., Lin, Y., Qing, J., An, Z. and Revenaugh, J.: A high-resolution, absolute-dated Holocene and deglacial Asian monsoon record from Dongge Cave, China, Earth Planet. Sci. Lett., 233(1–2), 71–86, https://doi.org/10.1016/J.EPSL.2005.01.036, 2005.

595 Eltahir, E. A. B. and Bras, R. L.: Precipitation recycling in the Amazon basin, Q. J. R. Meteorol. Soc., 120(518), 861–880, https://doi.org/10.1002/qj.49712051806, 1994.

Fairchild, I. J. and Baker, A.: Speleothem Science: From Process to Past Environments, 1st ed., Wiley-Blackwell, Chichester., 2012.

Fleitmann, D., Burns, S. J., Neff, U., Mudelsee, M., Mangini, A. and Matter, A.: Palaeoclimatic interpretation of high-600 resolution oxygen isotope profiles derived from annually laminated speleothems from Southern Oman, Quat. Sci. Rev., 23(7–8), 935–945, https://doi.org/10.1016/j.quascirev.2003.06.019, 2004.

Friedman, I., Harris, J. M., Smith, G. I. and Johnson, C. A.: Stable isotope composition of waters in the Great Basin, United States 1. Air-mass trajectories, J. Geophys. Res. Atmos., https://doi.org/10.1029/2001JD000565, 2002.

Gat, J. R.: Oxygen and hydrogen isotopes in the hydrological cycle, Annu. Rev. Earth Planet. Sci., 24(1), 225–262, 605 https://doi.org/10.1146/annurev.earth.24.1.225, 1996.

Gierz, P., Werner, M. and Lohmann, G.: Simulating climate and stable water isotopes during the last interglacial using a coupled climate-isotope model, link to model results, PANGAEA, https://doi.org/10.1594/PANGAEA.879229, 2017a.

Gierz, P., Werner, M. and Lohmann, G.: Simulating climate and stable water isotopes during the Last Interglacial using a coupled climate-isotope model, J. Adv. Model. Earth Syst., 9(5), 2027–2045, https://doi.org/10.1002/2017MS001056, 2017b.

610 Gower, J. C.: Some distance properties of latent root and vector methods used in multivariate analysis, Biometrika, 53(3–4), 325–338, https://doi.org/10.2307/2333639, 1966.

Griffiths, M. L., Drysdale, R. N., Gagan, M. K., Zhao, J. X., Ayliffe, L. K., Hellstrom, J. C., Hantoro, W. S., Frisia, S., Feng, Y. X., Cartwright, I., Pierre, E. S., Fischer, M. J. and Suwargadi, B. W.: Increasing Australian-Indonesian monsoon rainfall linked to early Holocene sea-level rise, Nat. Geosci., 2(9), 636–639, https://doi.org/10.1038/ngeo605, 2009.

615 Grossman, E. L. and Ku, T. L.: Oxygen and carbon isotope fractionation in biogenic aragonite: Temperature effects, Chem. Geol. Isot. Geosci. Sect., 59(1), 59–74, https://doi.org/10.1016/0168-9622(86)90057-6, 1986.

Haese, B., Werner, M. and Lohmann, G.: Stable water isotopes in the coupled atmosphere-land surface model ECHAM5-JSBACH, Geosci. Model Dev., 6, 3375–3418, https://doi.org/10.5194/gmd-6-1463-2013, 2012.

Hardy, D. R., Vuille, M. and Bradley, R. S.: Variability of snow accumulation and isotopic composition on Nevado Sajama, 620 Bolivia, J. Geophys. Res. D Atmos., 108(D22), https://doi.org/10.1029/2003jd003623, 2003.

Harris, I., Jones, P. D., Osborn, T. J. and Lister, D. H.: Updated high-resolution grids of monthly climatic observations - the

CRU TS3.10 Dataset, Int. J. Climatol., 34(3), 623–642, https://doi.org/10.1002/joc.3711, 2014.

Hong, Y. T., Hong, B., Lin, Q. H., Zhu, Y. X., Shibata, Y., Hirota, M., Uchida, M., Leng, X. T., Jiang, H. B., Xu, H., Wang, H. and Yi, L.: Correlation between Indian Ocean summer monsoon and North Atlantic climate during the Holocene, Earth Planet. Sci. Lett., 211(3–4), 371–380, https://doi.org/10.1016/S0012-821X(03)00207-3, 2003.

Hu, J., Emile-Geay, J., Tabor, C., Nusbaumer, J. and Partin, J.: Deciphering oxygen isotope records from Chinese speleothems with an isotope-enabed climate model, Paleoceanogr. Paleoclimatology, 43(12), 2098-2112, https://doi.org/ 10.1029/2019PA003741, 2019.

IAEA/WMO: Global Network of Isotopes in Precipitation, The GNIP Database, available at: http://www.iaea.org/water (last access: 20 January 2019), 2018.

Indermühle, A., Stocker, T. F., Joos, F., Fischer, H., Smith, H. J., Wahlen, M., Deck, B., Mastroianni, D., Tschumi, J., Blunier, T., Meyer, R. and Stauffer, B.: Holocene carbon-cycle dynamics based on CO_2 trapped in ice at Taylor Dome, Antarctica, Nature, 398(6723), 121–126, https://doi.org/10.1038/18158, 1999.

Kanner, L. C., Burns, S. J., Cheng, H., Edwards, R. L. and Vuille, M.: High-resolution variability of the South American summer monsoon over the last seven millennia: Insights from a speleothem record from the central Peruvian Andes, Quat. Sci. Rev., 75, 1–10, https://doi.org/10.1016/j.quascirev.2013.05.008, 2013.

Kärkkäinen T. and Saarela M.: Robust Principal Component Analysis of Data with Missing Values. In: Perner P. (eds) Machine Learning and Data Mining in Pattern Recognition. MLDM 2015. Lecture Notes in Computer Science, vol 9166. Springer, Cham, 2015

Kathayat, G., Cheng, H., Sinha, A., Spötl, C., Edwards, R. L., Zhang, H., Li, X., Yi, L., Ning, Y., Cai, Y., Lui, W. L. and Breitenbach, S. F. M.: Indian monsoon variability on millennial-orbital timescales, Sci. Rep., 6, 24374, https://doi.org/10.1038/srep24374, 2016.

Kaushal, N., Breitenbach, S. F. M., Lechleitner, F. A., Sinha, A., Tewari, V. C., Ahmad, S. M., Berkelhammer, M., Band, S., Yadava, M., Ramesh, R. and Henderson, G. M.: The Indian Summer Monsoon from a Speleothem $\delta^{18}O$ Perspective—A Review, Quaternary, 1(3), 29, https://doi.org/10.3390/quat1030029, 2018.

Kennett, D. J., Breitenbach, S. F. M., Aquino, V. V., Asmerom, Y., Awe, J., Baldini, J. U. L., Bartlein, P., Culleton, B. J., Ebert, C., Jazwa, C., Macri, M. J., Marwan, N., Polyak, V., Prufer, K. M., Ridley, H. E., Sodemann, H., Winterhalder, B. and Haug, G. H.: Development and disintegration of Maya political systems in response to climate change, Science, 338(6108), 788–791, https://doi.org/10.1126/science.1226299, 2012.

Krause, C. E., Gagan, M. K., Dunbar, G. B., Hantoro, W. S., Hellstrom, J. C., Cheng, H., Edwards, R. L., Suwargadi, B. W., Abram, N. J. and Rifai, H.: Spatio-temporal evolution of Australasian monsoon hydroclimate over the last 40,000 years, Earth Planet. Sci. Lett., 513, 103–112, https://doi.org/10.1016/j.epsl.2019.01.045, 2019.

Kuhnt, W., Holbourn, A., Xu, J., Opdyke, B., De Deckker, P., Röhl, U. and Mudelsee, M.: Southern Hemisphere control on Australian monsoon variability during the late deglaciation and Holocene, Nat. Commun., 6(1), 1–7, https://doi.org/10.1038/ncomms6916, 2015.

Kutzbach, J., Bonan, G., Foley, J. and Harrison, S. P.: Vegetation and soil feedbacks on the response of the African monsoon to orbital forcing in the early to middle Holocene, Nature, 384(6610), 623–626, https://doi.org/10.1038/384623a0, 1996.

Kutzbach, J. E., Liu, X., Liu, Z. and Chen, G.: Simulation of the evolutionary response of global summer monsoons to orbital

forcing over the past 280,000 years, Clim. Dyn., 30(6), 567–579, https://doi.org/10.1007/s00382-007-0308-z, 2008.

660 Lachniet, M. S.: Climatic and environmental controls on speleothem oxygen-isotope values, Quat. Sci. Rev., 28(5–6), 412–432, https://doi.org/10.1016/j.quascirev.2008.10.021, 2009.

Lachniet, M. S.: Are aragonite stalagmites reliable paleoclimate proxies? Tests for oxygen isotope time-series replication and equilibrium, Bull. Geol. Soc. Am., 127(11–12), 1521–1533, https://doi.org/10.1130/B31161.1, 2015.

Langebroek, P. M., Werner, M. and Lohmann, G.: Climate information imprinted in oxygen-isotopic composition of
665 precipitation in Europe, Earth Planet. Sci. Lett., 311(1–2), 144–154, https://doi.org/10.1016/j.epsl.2011.08.049, 2011.

Legendre, P. and Legendre, L.: Numerical Ecology, 2nd edition, Elsevier B.V, Amsterdam., 1998.

LeGrande, A. N. and Schmidt, G. A.: Sources of Holocene variability of oxygen isotopes in paleoclimate archives, Clim. Past, 5(3), 441–455, https://doi.org/10.5194/cp-5-441-2009, 2009.

Lewis, S. C., LeGrande, A. N., Kelley, M. and Schmidt, G. A.: Water vapour source impacts on oxygen isotope variability in
670 tropical precipitation during Heinrich events, Clim. Past, 6(3), 325–343, https://doi.org/10.5194/cp-6-325-2010, 2010.

Lewis, S. C., LeGrande, A. N., Schmidt, G. A. and Kelley, M.: Comparison of forced ENSO-like hydrological expressions in simulations of the preindustrial and mid-Holocene , J. Geophys, Res. Atmos., 119(12), 7064-7082, https://doi.org/10.1002/2013JD020961, 2014.

Licciardi, J. M., Clark, P. U., Jenson, J. W. and Macayeal, D. R.: Deglaciation of a soft-bedded Laurentide Ice Sheet, Quat.
675 Sci. Rev., 17(4–5), 427–448, https://doi.org/10.1016/S0277-3791(97)00044-9, 1998.

Maher, B. A.: Holocene variability of the East Asian summer monsoon from Chinese cave records: A re-assessment, Holocene, 18(6), 861–866, https://doi.org/10.1177/0959683608095569, 2008.

Maher, B. A.: Palaeoclimatic records of the loess/palaeosol sequences of the Chinese Loess Plateau, Quat. Sci. Rev., 154, 23–84, https://doi.org/10.1016/j.quascirev.2016.08.004, 2016.

680 Maher, B. A. and Thompson, R.: Oxygen isotopes from Chinese caves: Records not of monsoon rainfall but of circulation regime, J. Quat. Sci., 27(6), 615–624, https://doi.org/10.1002/jqs.2553, 2012.

Marlon, J. R., Bartlein, P. J., Carcaillet, C., Gavin, D. G., Harrison, S. P., Higuera, P. E., Joos, F., Power, M. J. and Prentice, I. C.: Climate and human influences on global biomass burning over the past two millennia, Nat. Geosci., 1(10), 697–702, https://doi.org/10.1038/ngeo313, 2008.

685 Marzin, C. and Braconnot, P.: Variations of Indian and African monsoons induced by insolation changes at 6 and 9.5 kyr BP, Clim. Dyn., 33(2–3), 215–231, https://doi.org/10.1007/s00382-009-0538-3, 2009.

McDermott, F.: Palaeo-climate reconstruction from stable isotope variations in speleothems: A review, Quat. Sci. Rev., 23(7–8), 901–918, https://doi.org/10.1016/j.quascirev.2003.06.021, 2004.

Misra, P., Tandon, S. K. and Sinha, R.: Holocene climate records from lake sediments in India: Assessment of coherence
690 across climate zones, Earth-Science Rev., 190, 370–397, https://doi.org/10.1016/j.earscirev.2018.12.017, 2019.

Mohtadi, M., Oppo, D. W., Steinke, S., Stuut, J. B. W., De Pol-Holz, R., Hebbeln, D. and Lückge, A.: Glacial to Holocene swings of the Australian-Indonesian monsoon, Nat. Geosci., 4(8), 540–544, https://doi.org/10.1038/ngeo1209, 2011.

Nivet, F., Bergonzini, L., Mathé, P. E., Noret, A., Monvoisin, G., Majule, A. and Williamson, D.: Influence of the balance of the intertropical front on seasonal variations of the isotopic composition in rainfall at Kisiba Masoko (Rungwe Volcanic Province, SW, Tanzania), Isotopes Environ. Health Stud., 54(4), 352–369, https://doi.org/10.1080/10256016.2018.1443923, 2018.

Oksanen, J., Blanchet, F. G., Friendly, M., Kindt, R., Legendre, P., McGlinn, D., Minchin, P. R., O'Hara, R. B., Simpson, G. L., Solymos, P., Stevens, M. H. H., Szoecs, E. and Wagner, H.: vegan: Community Ecology Package. R package version 2.5-2, Cran R, 2019.

Pausata, F. S. R., Battisti, D. S., Nisancioglu, K. H. and Bitz, C. M.: Chinese stalagmite $\delta^{18}O$ controlled by changes in the Indian monsoon during a simulated Heinrich event, Nat. Geosci., 4(7), 474–480, https://doi.org/10.1038/ngeo1169, 2011.

Quigley, M. C., Horton, T., Hellstrom, J. C., Cupper, M. L. and Sandiford, M.: Holocene climate change in arid Australia from speleothem and alluvial records, Holocene, 20(7), 1093–1104, https://doi.org/10.1177/0959683610369508, 2010.

R Core Team: R: A Language and Environment for Statistical Computing, [online] Available from: https://www.r-project.org/, 2019.

Rachmayani, R., Prange, M. and Schulz, M.: North African vegetation-precipitation feedback in early and mid-Holocene climate simulations with CCSM3-DGVM, Clim. Past, 11(2), https://doi.org/10.5194/cp-11-175-2015, 2015.

Rao, C. R.: The use and interpretation of principal component analysis in applied research, Sankhya Indian J. Stat. Ser. A, 329–358, 1964.

Risi, C., Bony, S. and Vimeux, F.: Influence of convective processes on the isotopic composition ($\delta^{18}O$ and δD) of precipitation and water vapor in the tropics: 2. Physical interpretation of the amount effect, J. Geophys. Res. Atmos., 113(D19), https://doi.org/10.1029/2008JD009943, 2008.

Risi, C., Bony, S., Vimeux, F. and Jouzel, J.: Water-stable isotopes in the LMDZ4 general circulation model: Model evaluation for present-day and past climates and applications to climatic interpretations of tropical isotopic records, J. Geophys. Res. Atmos., 115(D12), https://doi.org/10.1029/2009JD013255, 2010.

Rohlf, F.J.: An Empirical Comparison of Three Ordination Techniques in Numerical Taxonomy, Syst. Biol., 21, 271–280, https://doi.org/10.1093/sysbio/21.3.271, 1972.

Rozanski, K., Araguás-Araguás, L. and Gonfiantini, R.: Isotopic patterns in modern global precipitation, Geophys Monogr., 78, 1–36, https://doi.org/10.1029/GM078p0001, 1993.

Salati, E., Dall'Olio, A., Matsui, E. and Gat, J. R.: Recycling of water in the Amazon Basin: An isotopic study, Water Resour. Res., 15(5), 1250–1258, https://doi.org/10.1029/WR015i005p01250, 1979.

Schäfer-Neth, C. and Paul, A.: The Atlantic Ocean at the Last Glacial Maximum: 1. Objective mapping of the GLAMAP sea-surface conditions, in The South Atlantic in the Late Quaternary, edited by G. Wefer, S. Mulitza, and V. Ratmeyer, pp. 531–548, Springer, Berlin, Heidelberg., 2003.

Sowers, T.: Ice core records of atmospheric N_2O covering the last 106,000 years, Science, 301(5635), 945–948, https://doi.org/10.1126/science.1085293, 2003.

Steinke, S., Mohtadi, M., Prange, M., Varma, V., Pittauerova, D. and Fischer, H. W.: Mid- to Late-Holocene Australian-Indonesian summer monsoon variability, Quat. Sci. Rev., 93, 142–154, https://doi.org/10.1016/j.quascirev.2014.04.006, 2014.

Tan, M.: Circulation effect: Response of precipitation δ¹⁸O to the ENSO cycle in monsoon regions of China, Clim. Dyn., 42(3–4), 1067–1077, https://doi.org/10.1007/s00382-013-1732-x, 2014.

Tremaine, D. M., Froelich, P. N. and Wang, Y.: Speleothem calcite farmed in situ: Modern calibration of δ¹⁸O and δ¹³C paleoclimate proxies in a continuously-monitored natural cave system, Geochim. Cosmochim. Acta, 75(17), 4929–4950, https://doi.org/10.1016/j.gca.2011.06.005, 2011.

Trenberth, K. E., Stepaniak, D. P. and Caron, J. M.: The global monsoon as seen through the divergent atmospheric circulation, J. Clim., 13(22), 3969–3993, https://doi.org/10.1175/1520-0442(2000)013<3969:TGMAST>2.0.CO;2, 2000.

Varma, V., Prange, M., Merkel, U., Kleinen, T., Lohmann, G., Pfeiffer, M., Renssen, H., Wagner, A., Wagner, S. and Schulz, M.: Holocene evolution of the Southern Hemisphere westerly winds in transient simulations with global climate models, Clim. Past, 8, 391–402, https://doi.org/10.5194/cp-8-391-2012, 2012.

Wackerbarth, A., Langebroek, P. M., Werner, M., Lohmann, G., Riechelmann, S., Borsato, A. and Mangini, A.: Simulated oxygen isotopes in cave drip water and speleothem calcite in European caves, Clim. Past, 8(6), 1781–1799, https://doi.org/10.5194/cp-8-1781-2012, 2012.

Waelbroeck, C., Labeyrie, L., Michel, E., Duplessy, J. C., McManus, J. F., Lambeck, K., Balbon, E. and Labracherie, M.: Sea-level and deep water temperature changes derived from benthic foraminifera isotopic records, Quat. Sci. Rev., 21(1–3), 295–305, https://doi.org/10.1016/S0277-3791(01)00101-9, 2002.

Wang, P. X., Wang, B., Cheng, H., Fasullo, J., Guo, Z. T., Kiefer, T. and Liu, Z. Y.: The global monsoon across timescales: Coherent variability of regional monsoons, Clim. Past, 10(6), 2007–2052, https://doi.org/10.5194/cp-10-2007-2014, 2014.

Wang, X., Auler, A. S., Edwards, R. L., Cheng, H., Ito, E. and Solheid, M.: Interhemispheric anti-phasing of rainfall during the last glacial period, Quat. Sci. Rev., 25(23–24), 3391–3403, https://doi.org/10.1016/j.quascirev.2006.02.009, 2006.

Wang, Y., Cheng, H., Edwards, R. L., Kong, X., Shao, X., Chen, S., Wu, J., Jiang, X., Wang, X. and An, Z.: Millennial- and orbital-scale changes in the East Asian monsoon over the past 224,000 years, Nature, 451(7182), 1090–1093, https://doi.org/10.1038/nature06692, 2008.

Wang, Y. J., Cheng, H., Edwards, R. L., An, Z. S., Wu, J. Y., Shen, C. C. and Dorale, J. A.: A high-resolution absolute-dated late Pleistocene monsoon record from Hulu Cave, China, Science, 294(5550), 2345–2348, https://doi.org/10.1126/science.1064618, 2001.

Waterisotopes Database: http://wateriotopes.org, last access: 15 April 2017.

Werner, M.: ECHAM5-wiso simulation data – present-day, mid-Holocene, and Last Glacial Maximum, PANGAEA, https://doi.org/https://doi.pangaea.de/10.1594/PANGAEA.902347, 2019.

Werner, M., Langebroek, P. M., Carlsen, T., Herold, M. and Lohmann, G.: Stable water isotopes in the ECHAM5 general circulation model: Toward high-resolution isotope modeling on a global scale, J. Geophys. Res. Atmos., 116(D15), https://doi.org/10.1029/2011JD015681, 2011.

Werner, M., Haese, B., Xu, X., Zhang, X., Butzin, M. and Lohmann, G.: Glacial-interglacial changes in H₂¹⁸O, HDO and deuterium excess-results from the fully coupled ECHAM5/MPI-OM Earth system model, Geosci. Model Dev., 9(2), 647–670, https://doi.org/10.5194/gmd-9-647-2016, 2016.

Werner, M., Jouzel, J., Masson-Delmotte, V. and Lohmann, G.: Reconciling glacial Antarctic water stable isotopes with ice

765   sheet topography and the isotopic paleothermometer, Nat. Commun., 9(1), 1–10, https://doi.org/10.1038/s41467-018-05430-y, 2018.

Wickham, H.: ggplot2: Elegant Graphics for Data Analysis, Springer-Verlag, New York. [online] Available from: https://ggplot2.tidyverse.org, 2016.

Wurtzel, J. B., Abram, N. J., Lewis, S. C., Bajo, P., Hellstrom, J. C., Troitzsch, U. and Heslop, D.: Tropical Indo-Pacific
770   hydroclimate response to North Atlantic forcing during the last deglaciation as recorded by a speleothem from Sumatra, Indonesia, Earth Planet. Sci. Lett., 492, 264–278, https://doi.org/10.1016/j.epsl.2018.04.001, 2018.

Wyrwoll, K. H. and Miller, G. H.: Initiation of the Australian summer monsoon 14,000 years ago, Quat. Int., 83, 119–128, https://doi.org/10.1016/S1040-6182(01)00034-9, 2001.

Xu, X., Werner, M., Butzin, M. and Lohmann, G.: Water isotope variations in the global ocean model MPI-OM, Geosci. Model
775   Dev., 5(3), 809–818, https://doi.org/10.5194/cpd-8-4885-2012, 2012.

Yang, X., Liu, J., Liang, F., Yuan, D., Yang, Y., Lu, Y. and Chen, F.: Holocene stalagmite δ^{18}O records in the East Asian monsoon region and their correlation with those in the Indian monsoon region, Holocene, 24(12), 1657–1664, https://doi.org/10.1177/0959683614551222, 2014.

Yonge, C. J., Ford, D. C., Gray, J. and Schwarcz, H. P.: Stable isotope studies of cave seepage water, Chem. Geol. Isot. Geosci.
780   Sect., 58(1–2), 97–105, https://doi.org/10.1016/0168-9622(85)90030-2, 1985.

Yuan, D., Cheng, H., Edwards, R. L., Dykoski, C. A., Kelly, M. J., Zhang, M., Qing, J., Lin, Y., Wang, Y., Wu, J., Dorale, J. A., An, Z. and Cai, Y.: Timing, duration, and transitions of the Last Interglacial Asian monsoon, Science, 304(5670), 575–578, https://doi.org/10.1126/science.1091220, 2004.

Yue, X., Wang, H., Liao, H. and Jiang, D.: Simulation of the Direct Radiative Effect of Mineral Dust Aerosol on the Climate
785   at the Last Glacial Maximum, J. Clim., 24(3), 843–858, https://doi.org/10.1175/2010JCLI3827.1, 2011.

Zhang, Brahim, Li, Zhao, Kathayat, Tian, Baker, Wang, Zhang, Ning, Edwards and Cheng: The Asian Summer monsoon: Teleconnections and forcing Mechanisms—A review from Chinese speleothem δ^{18}O records, Quaternary, 2(3), 26, https://doi.org/10.3390/quat2030026, 2019.

Zhang, X., Jin, L., Chen, J., Lu, H. and Chen, F.: Lagged response of summer precipitation to insolation forcing on the
790   northeastern Tibetan Plateau during the Holocene, Clim. Dyn., 50(9–10), 3117–3129, https://doi.org/10.1007/s00382-017-3784-9, 2018.

Zhao, Y. and Harrison, S. P.: Mid-Holocene monsoons: A multi-model analysis of the inter-hemispheric differences in the responses to orbital forcing and ocean feedbacks, Clim. Dyn., 39(6), 1457–1487, https://doi.org/10.1007/s00382-011-1193-z, 2012.

795   Zhou, W., Yu, X., Jull, A. J. T., Burr, G., Xiao, J. Y., Lu, X. and Xian, F.: High-resolution evidence from southern China of an early Holocene optimum and a mid-Holocene dry event during the past 18,000 years, Quat. Res., 62(1), 39–48, https://doi.org/10.1016/j.yqres.2004.05.004, 2004.

800
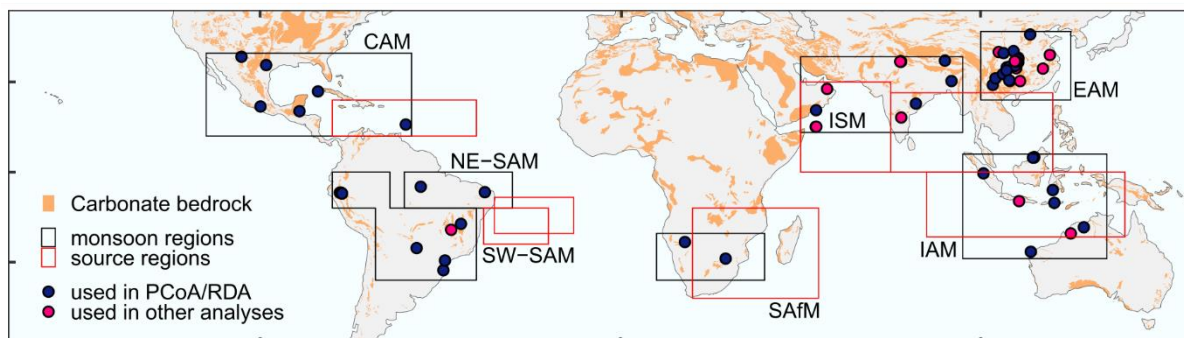
Figure 1: Spatial distribution of speleothem records used is this study. Colours indicate the sites used in Principle Coordinates Analysis and Redundancy Analysis (PCoA, RDA) to separate monsoon regions, and sites not used in PCoA and RDA but used in subsequent analyses. Boxes used in the allocation of sites into individual regional monsoons are shown: CAM = Central American Monsoon, SW-SAM = southwestern South American Monsoon, NE-SAM = northeastern South American Monsoon, SAfM = southern African Monsoon, ISM = Indian Summer Monsoon, EAM = East Asian Monsoon, IAM = Indonesian-Australian Monsoon. Source region limits used in the multiple linear regression analysis are also shown. The background carbonate lithology is from the World Karst Aquifer Mapping (WOKAM) project (Chen et al., 2017).
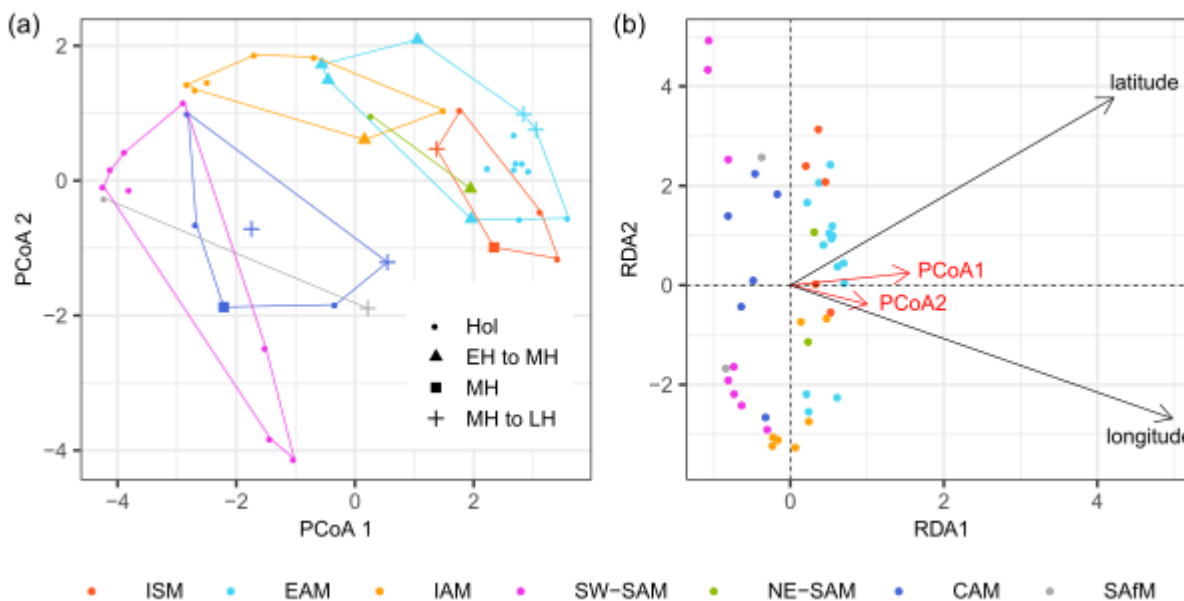
810

Figure 2: Results of Principle Coordinate Analysis (PCoA) and Redundancy analysis (RDA). (a) PCoA biplot showing the loadings of each site on the first 2 axes, which represent 85% of the total variance. Shapes indicate the Holocene coverage of each site, where sites with a coverage ≥ 8000 years represent most or all of the Holocene (Hol). Sites with a temporal coverage of < 8000 years are coded to show whether they represent the early to mid-Holocene (EH to MH, record midpoint > 8,000 years BP), the mid Holocene (MH, record midpoint between 8,000 and 5,000 years BP), or the mid to late-Holocene (LH to MH, midpoint <5,000 years BP). (b) RDA triplot, where the response variables are the PCoa1 and PCoA2 axes explained by latitude and longitude. The direction of the PCoA axes have been fixed so that they align with the explanatory variables.
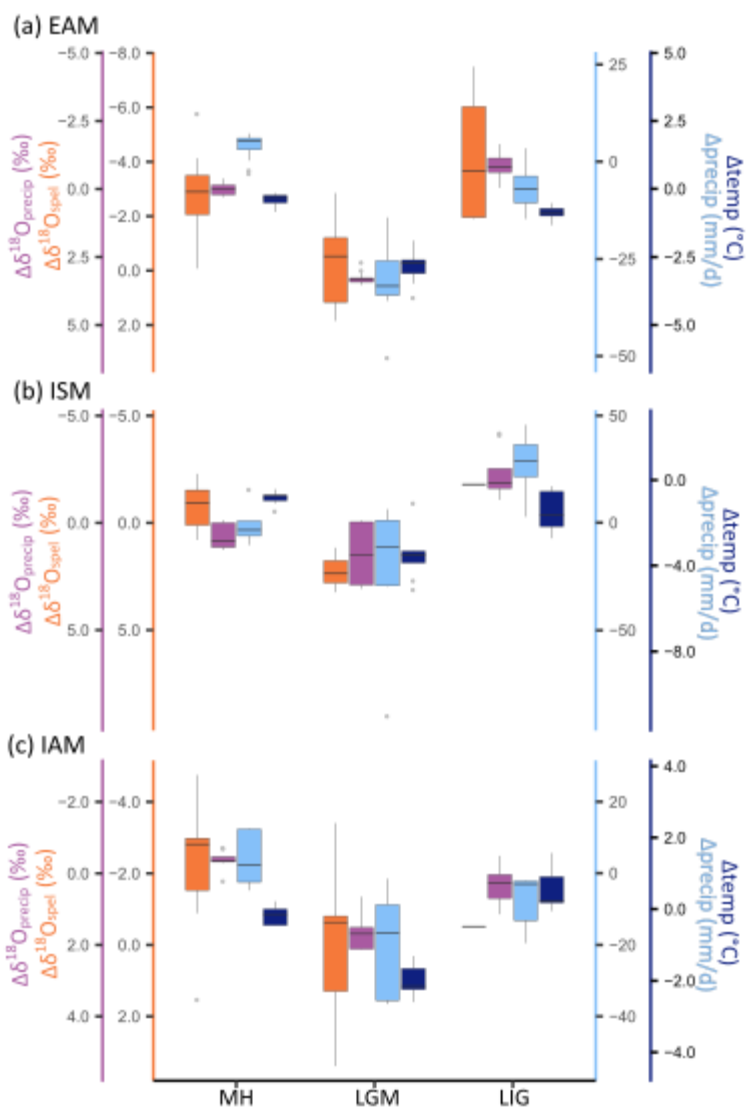
820   **Figure 3: Speleothem δ¹⁸O anomalies compared to anomalies of δ¹⁸O_precip, precipitation and temperature from the ECHAM simulations for the (a) East Asian (EAM), (b) Indian (ISM) and (c) Indonesian-Australian (IAM) monsoons. The boxes show the median value (line) and the interquartile range, and the whiskers shown the minimum and maximum values, with outliers represented by grey dots. Note that the isotope axes are reversed, so that the most negative anomalies are at the top of the plot, to be consistent with the assumed relationship with the direction of change in precipitation and temperature.**

825
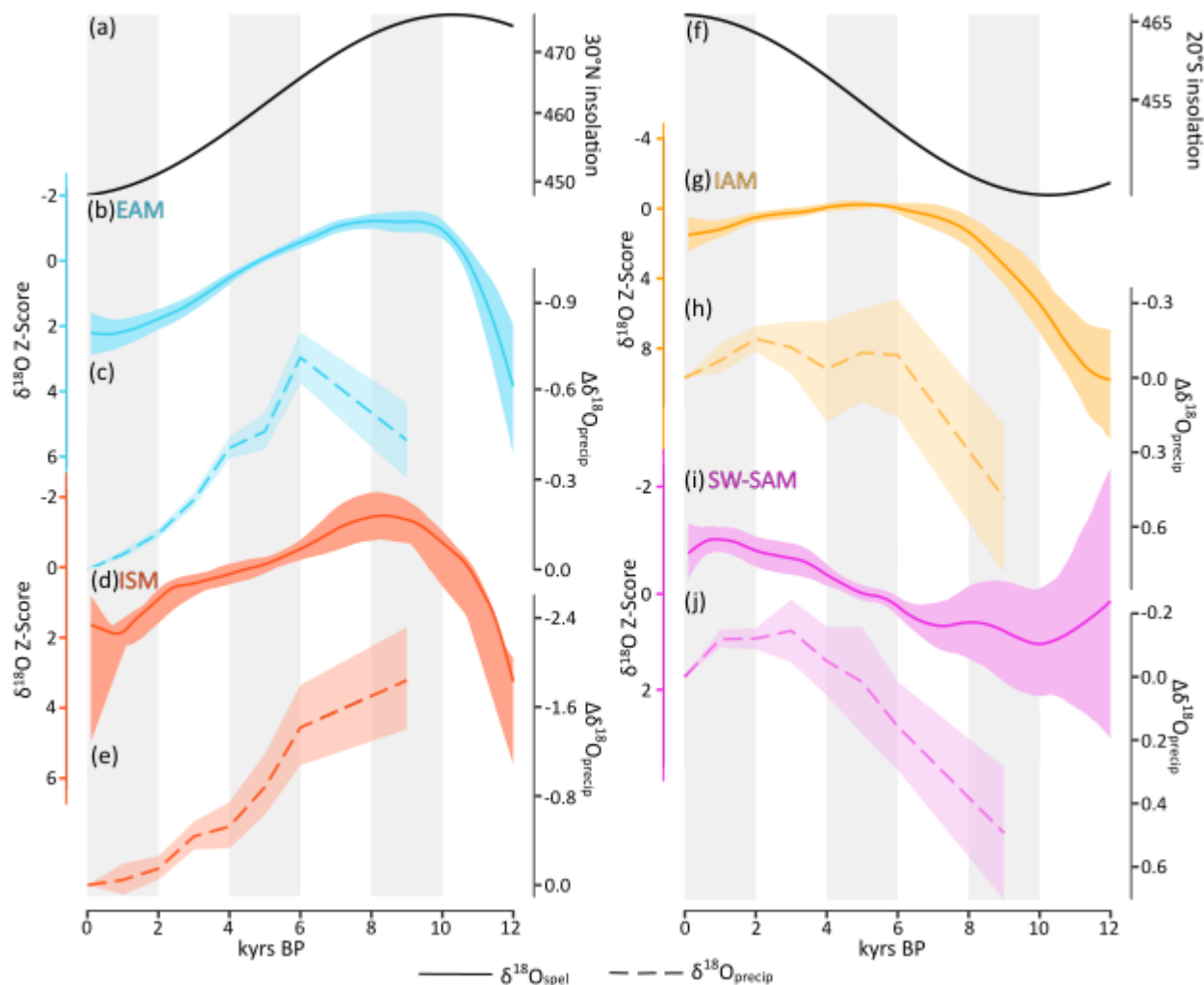
Figure 4: Evolution of regional speleothem δ¹⁸O signals through the Holocene compared to δ¹⁸Oprecip simulated by the GISS model. The left panel shows northern hemisphere monsoons (EAM = East Asian Monsoon; ISM = Indian Summer Monsoon) and summer (May through September) insolation at 30° N (Berger, 1978). The right panel shows southern hemisphere monsoons (SW-SAM = southwest South American Monsoon; IAM = Indonesian-Australian Monsoon) and summer (November through March) insolation for 20° S (Berger, 1978). The speleothem δ¹⁸O changes are expressed as z-scores, with a smoothed loess fit (3,000 year window), and confidence intervals obtained by bootstrapping by site. δ¹⁸Oprecip values are expressed as anomalies from the pre-industrial control simulation. Note that the isotope axes are reversed, so that the most negative anomalies are at the top of the plot, to be consistent with the assumed relationship with the changes in insolation.
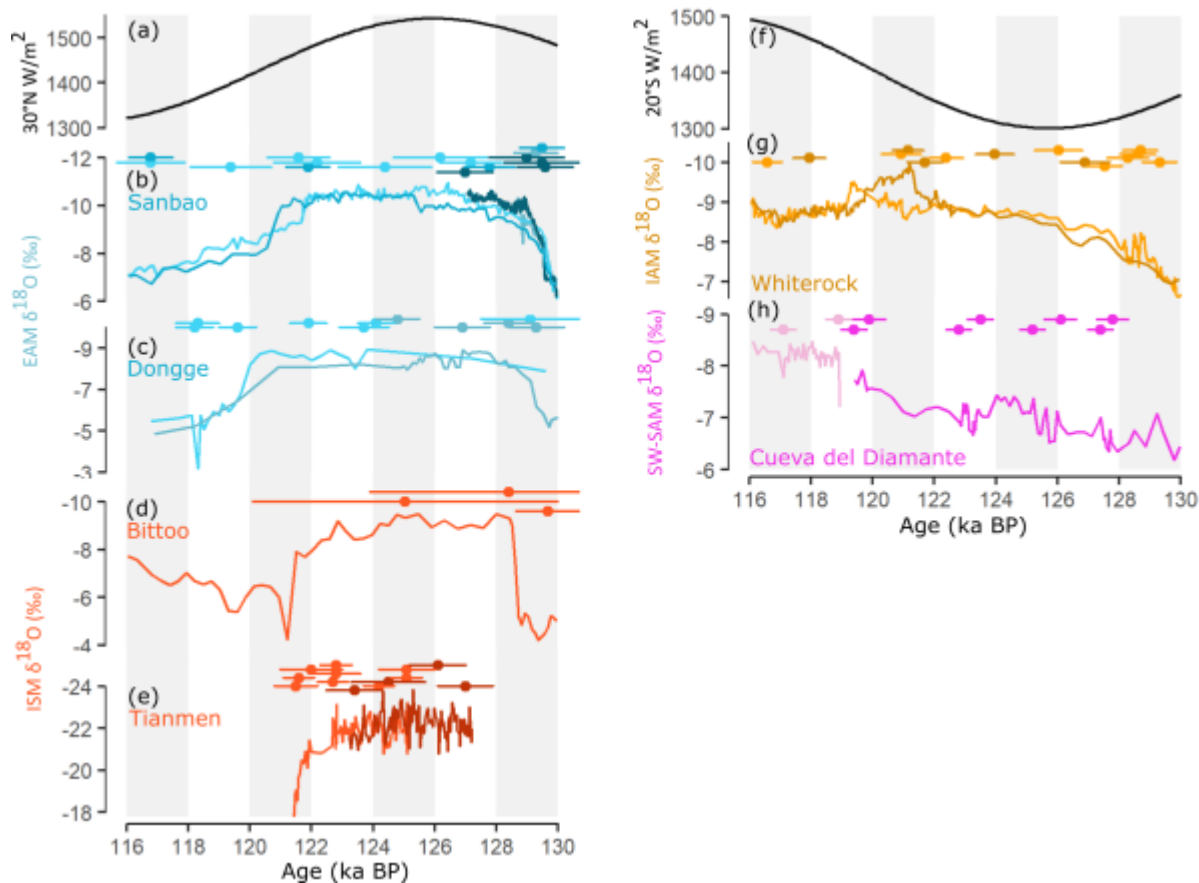
Figure 5: Comparison of changes in summer insolation and Last Interglacial δ¹⁸O_spel records from the (b,c) East Asian Monsoon (EAM), (d,e) Indian Summer Monsoon (ISM), (g) southwest South American Monsoon (SW-SAM) and (h) Indonesian-Australian Monsoon (IAM) regions. The U/Th dates and uncertainties are shown for each record. The summer insolation curves (Berger, 1978)

840 **are for May through September at 30° N in the northern hemisphere (a) and for November through March for 20° S in the southern hemisphere (f). Note that the isotope axes are reversed, so that the most negative anomalies are at the top of the plot, to be consistent with the assumed relationship with the changes in insolation.**
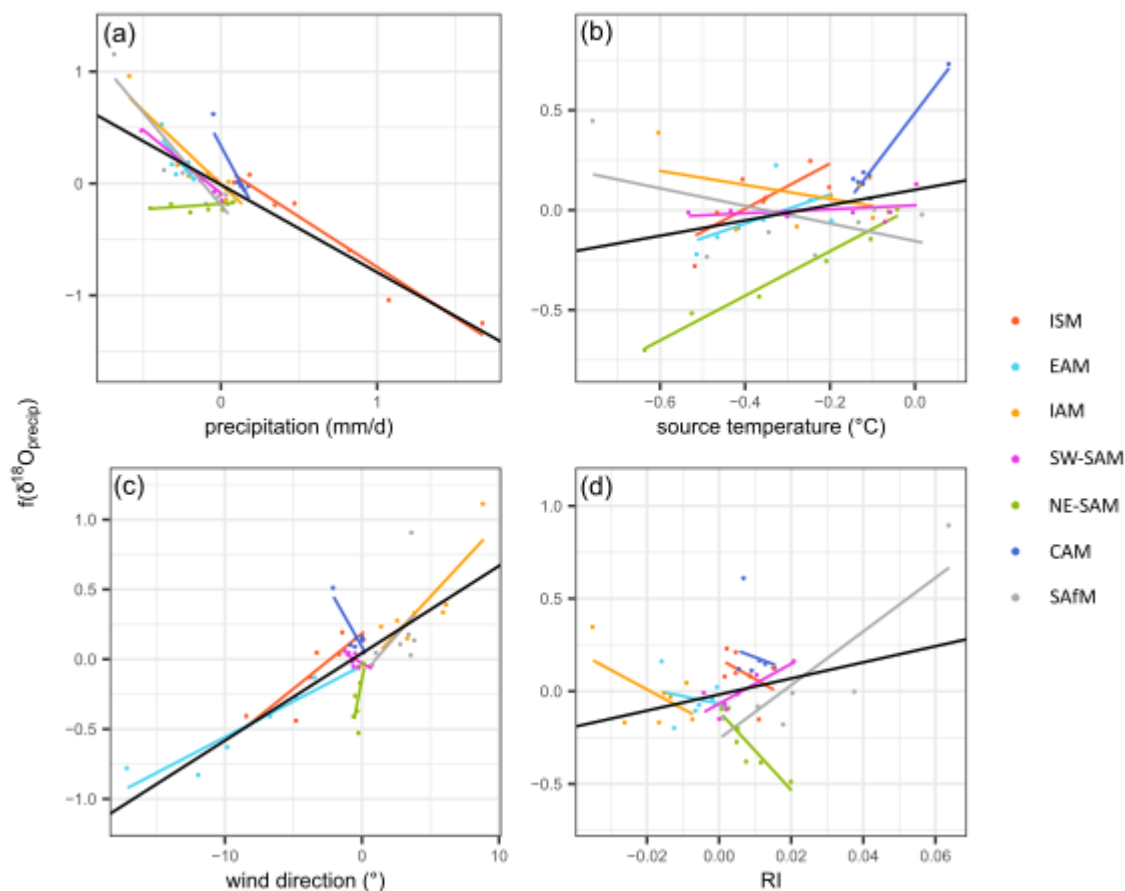
845 **Figure 6: Partial residual plots from the multiple linear regression analysis, showing the relationship between anomalies in simulated δ18Oprecip and the four predictor variables, after taking account of the fitted partial effects of all the other predictors. The simulated δ18Oprecip are anomalies relative to the pre-industrial control simulation, and are annual values weighted by precipitation amount. The predictor variables are: precipitation in the delineated monsoon region (mm/d), temperature in the source region (°C), surface wind direction over the source region (°) as an index of potential changes in source region and the ratio of precipitation recycling to**
850 **total precipitation over the monsoon region (RI, unitless). The predictor variables are summer mean values, where summer is defined as May to September for northern hemisphere monsoons and November to March for southern hemisphere monsoons.**

	PCoA1	PCoA2	PCoA3	PCoA4	PCoA5
Eigenvalue	**269.0586**	**85.22482**	16.81258	10.25072	5.552469
Explained (%)	**64.87459**	**20.54915**	4.053797	2.471623	1.338794
Cumulative (%)	**64.87459**	**85.42374**	89.47753	91.94916	93.28795

Table 1: Results of the Principle Coordinates Analysis (PCoA). Significant axes, as determined by the broken stick method (Bennett, 1996), are shown in bold.

855

	RDA1	RDA2
Latitude	**0.88**	-0.47
Longitude	**0.75**	0.67
Eigenvalue	0.73	0.04
Explained (%)	36.7	2.2

Table 2: Results of the redundancy analysis (RDA). Variables that are significantly correlated (P <0.01) with the RDA axes are shown in bold.

	Regression coefficient	T value
Regional precipitation	**-0.16**	-8.75
Source area temperature	**0.39**	2.05
Wind direction	**0.06**	8.03
Precipitation recycling	4.34	1.92

860 **Table 3: Results of the multiple linear regression analysis. Significant relationships (P > 0.01) are shown in bold.**

865